A SIMPLE TECHNIQUE FOR PREDICTING HIGH-REDSHIFT GALAXY EVOLUTION

PETER S. BEHROOZI[1] AND JOSEPH SILK[2,3,4]
[1] Space Telescope Science Institute, Baltimore, MD 21218, USA
[2] Institut d'Astrophysique, UMR 7095 CNRS, Université Pierre et Marie Curie, 98bis Boulevard Arago, F-75014 Paris, France
[3] Department of Physics and Astronomy, Johns Hopkins University, Baltimore, MD 21218, USA
[4] Beecroft Institute of Particle Astrophysics and Cosmology, Department of Physics, University of Oxford, Oxford OX1 3RH, UK

ABSTRACT

We show that the ratio of galaxies' specific star formation rates (SSFRs) to their host halos' specific mass accretion rates (SMARs) strongly constrains how the galaxies' stellar masses, SSFRs, and host halo masses evolve over cosmic time. This evolutionary constraint provides a simple way to probe $z > 8$ galaxy populations without direct observations. Tests of the method with galaxy properties at $z = 4$ successfully reproduce the known evolution of the stellar mass–halo mass (SMHM) relation, galaxy SSFRs, and the cosmic star formation rate (CSFR) for $5 < z < 8$. We then predict the continued evolution of these properties for $8 < z < 15$. In contrast to the nonevolution in the SMHM relation at $z < 4$, the median galaxy mass at fixed halo mass increases strongly at $z > 4$. We show that this result is closely linked to the flattening in galaxy SSFRs at $z > 2$ compared to halo SMARs; we expect that average galaxy SSFRs at fixed stellar mass will continue their mild evolution to $z \sim 15$. The expected CSFR shows no breaks or features at $z > 8.5$; this constrains both reionization and the possibility of a steep falloff in the CSFR at $z = 9$–10. Finally, we make predictions for stellar mass and luminosity functions for the *James Webb Space Telescope*, which should be able to observe one galaxy with $M_* \gtrsim 10^8 \, M_\odot$ per 10^3 Mpc^3 at $z = 9.6$ and one such galaxy per 10^4 Mpc^3 at $z = 15$.

Key words: dark matter – galaxies: abundances – galaxies: evolution

1. INTRODUCTION

The *James Webb Space Telescope* (*JWST*; launch: 2018) will strongly constrain galaxy formation from $z = 20$ to $z = 8$ (Gardner et al. 2006). Population III stars, globular clusters, supermassive black hole seeds, and the first galaxies are all expected to have formed during this epoch (see Bromm & Yoshida 2011 for a review). Early galaxies are also expected to reionize the intergalactic medium (see Loeb & Barkana 2001; Haardt & Madau 2012 for reviews). Yet, constraints on how many $z > 8$ galaxies *JWST* will observe have been contradictory. Some observations with the *Hubble Space Telescope* (*HST*) show a deficiency of star-forming galaxies at $z = 9$ and above (Ellis et al. 2013; Oesch et al. 2014b). However, *HST* imaging of clusters has returned evidence for both steeply declining and mildly evolving cosmic star formation rates (CSFRs; Bouwens et al. 2014a; Coe et al. 2013; Zheng et al. 2014; Oesch et al. 2014a). And to date, long gamma-ray bursts detected with *Swift* (which measure the total CSFR, as opposed to only star formation above a threshold) suggest only mild evolution in the total CSFR at $z > 8$ (Robertson & Ellis 2012; Kistler et al. 2013; Wang 2013);

Resolving this discrepancy by observing more $z > 8$ galaxies is difficult with current instruments. Indirect approaches based on existing measurements of $z = 7$ and $z = 8$ galaxies (Bradley et al. 2012; Schmidt et al. 2014; Bouwens et al. 2014c) represent an alternative. Stars formed at $z = 15$ or $z = 10$ are still present in $z = 7$–8 galaxies, so at the most basic level, a measurement of the current specific star formation rate (SSFR) can be used to guess how many stars were in place at earlier times (see, e.g., Leitner 2012). Yet, the strong connection between galaxy growth and the growth of collapsed, self-bound, virialized dark matter structures (i.e., "halos") in the Lambda cold dark matter (ΛCDM) paradigm (More et al. 2009; Yang et al. 2009; Leauthaud et al. 2012; Reddick et al. 2013; Tinker et al. 2013; Behroozi et al. 2013b) suggests that a more physical extrapolation can be made.

Previous theoretical work on the growth of galaxies in dark matter halos at high redshift has included hydrodynamical simulations (e.g., Finlator et al. 2011; Wise et al. 2012a, 2012b, 2014; Jaacks et al. 2012a, 2012b; Dayal et al. 2013), semi-analytical models (e.g., Lacey et al. 2011), and semiempirical models (e.g., Trenti et al. 2010; Tacchella et al. 2013; Wyithe et al. 2014). These models have tended to require significant assumptions for how galaxy luminosity is connected to dark matter halo properties, imposed either indirectly (through subgrid models in hydrodynamical simulations) or directly (as in a constant halo mass–luminosity relation in Trenti et al. 2010, or as in the semianalytical models in Lacey et al. 2011). Although the accuracy of existing luminosity functions at $z > 8$ is disputed (as noted above), some of these models predict a sharp decline in the CSFR above $z = 8$ owing to the lack of galaxies above the *HST* observational threshold (Trenti et al. 2010; Finlator et al. 2011; Jaacks et al. 2012a; Dayal et al. 2013).

We adopt an approach with somewhat weaker assumptions, which constrains how the relative growth of galaxies (i.e., their SSFRs) relates to the relative growth of their dark matter halos (i.e., their specific halo mass accretion rates). We show that the ratio of these two quantities predicts the trajectory along which high-redshift galaxies evolve in the stellar mass–halo mass (SMHM) plane—i.e., it constrains the historical SMHM relationship. As we will discuss, this relationship is valuable not only for predicting high-redshift and faint galaxy properties but also for understanding the SSFR "plateau"—that is, why galaxy SSFRs at fixed stellar mass are relatively flat at $z > 2$ (Weinmann et al. 2011). In addition, the connection to SSFRs also offers a better understanding of why the SMHM relationship appears to evolve at redshifts $z > 4$ (Behroozi et al. 2013c) but remains relatively constant for $z < 4$ (Behroozi et al. 2013b).

We describe the details of our approach in Section 2, discuss existing constraints from observations and simulations in Section 3, present tests and error analyses of the approach in

1

Section 4, and present results for $z > 8$ galaxy populations in Section 5. We discuss how these results affect the SSFR "plateau," dwarf galaxy star formation efficiency, abundance matching (including the "too big to fail" problem), reionization, and expectations for the *JWST* in Section 6. Finally, we summarize conclusions in Section 7. Our adopted cosmology is a flat, ΛCDM universe with $\Omega_M = 0.27$, $\Omega_b = 0.045$, $h = 0.7$, $\sigma_8 = 0.82$, and $n_s = 0.95$; these are very similar to the *WMAP9* best-fit parameters (Bennett et al. 2013). Throughout this paper we use the virial spherical overdensity definition in Bryan & Norman (1998) for halo masses.

2. THEORY

2.1. Basic Principles

Galaxy star formation histories are typically parameterized as a function of time, i.e., SFR(t). Yet, physically interpreting SFR(t) is not straightforward because changes in SFR with time come from both the large-scale environment (e.g., the redshift dependence of mass accretion rates) and local properties (e.g., host halo mass and gravitational potential well depth). We therefore consider a more physical parameterization that separates these two effects.

Galaxies at time t_f in a given stellar mass bin will have a well-defined average stellar mass, $M_{*,f}$, and a well-defined average halo mass, $M_{h,f}$. The halo mass is determinable through abundance matching/modeling if it is not known through other means (Section 3.2). In this paper we parameterize the average growth of the galaxies in terms of the average growth of their host dark matter halos, i.e., as $M_*(M_h(t))$. The changing cosmological accretion rate is captured in the average halo mass growth history, $M_h(t)$. The historical efficiency with which the galaxies converted infalling baryons into stars is captured in how M_* depends on M_h. We can write the galaxies' average star formation histories in terms of $M_*(M_h)$ as

$$\text{SFR}(M_h(t)) = \frac{dM_*}{dt} = \frac{dM_*}{dM_h}\frac{dM_h}{dt}. \tag{1}$$

Just as for SFR(t)-parameterized star formation histories, the form of $M_*(M_h)$ will depend on the redshift and stellar mass of the galaxies in question.[5]

As with fitting SFR(t) directly, we have to make an assumption about the functional form of $M_*(M_h)$. Regardless of its true form, we can approximate the recent stellar mass–halo mass history as a power law. This form is especially reasonable for galaxies at $z > 4$, which are typically not massive enough to experience active galactic nucleus (AGN) feedback and so only experience stellar feedback (supernovae and reionization) over much of their growth histories. We also test this assumption directly in Section 4 for galaxies from $z = 4$ to $z = 8$. Hence, we let

$$M_*(M_h) = M_{*,f}\left(\frac{M_h}{M_{h,f}}\right)^{\alpha}, \tag{2}$$

where α is the unknown power-law dependence. We reemphasize that Equation (2) describes the historical evolution of a galaxy population, so α differs from the local slope of the SMHM relation at time t_f if (and only if) the SMHM relation is evolving with redshift.

---

[5] We note that stellar mass loss (through supernovae and stellar winds) and stellar mass gain through mergers will also change M_*. These effects cancel to within 10% (see Section 2.2 and Figure 2), so we continue to write SFR($M_h(t)$) = (dM_*/dt) in this section for pedagogical clarity.
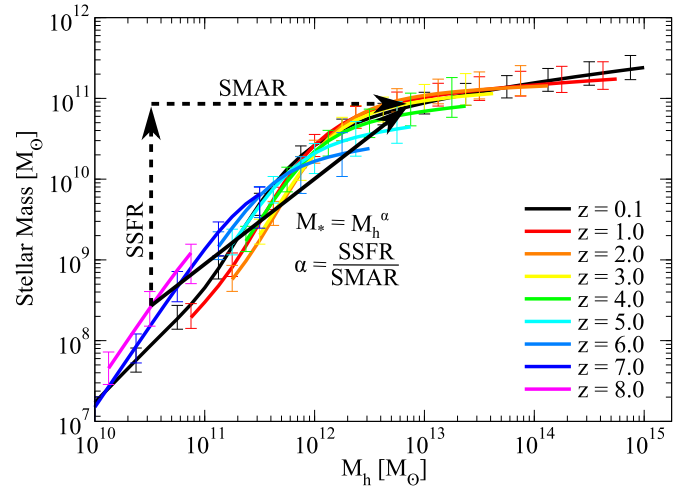

Figure 1. Galaxy evolution in the SMHM plane. The background figure shows the SMHM relations from $z = 8$ to $z = 0$ from Behroozi et al. (2013c). Evolution in this plane is set by two factors. Galaxies' SSFRs set the rate at which they increase in log stellar mass. Similarly, their SMARs set the rate at which they increase in log halo mass. The power-law slope of their future SMHM trajectory is therefore set by the ratio of their SSFRs to their SMARs, recalling that this slope equals rise (SSFR) over run (SMAR). Combining measured SSFRs with halo mass accretion histories from simulations therefore lets one predict galaxies' previous evolution in the SMHM plane.

Combining Equation (2) with Equation (1), the SFR history becomes a simple expression:

$$\text{SFR}(t) = \frac{\alpha M_*}{M_h}\frac{dM_h}{dt}. \tag{3}$$

Letting SSFR(t) be the SSFR ($M_*^{-1}(dM_*/dt)$) as a function of time, and letting SMAR(t) be the halo specific mass accretion rate (SMAR) ($M_h^{-1}(dM_h/dt)$), the beautiful symmetry in Equation (3) is apparent:

$$\frac{\text{SSFR}(t)}{\text{SMAR}(t)} = \alpha. \tag{4}$$

That is, the ratio of a galaxy population's average SSFR to its average specific host halo mass accretion rate will be constant, under the weak assumption that the recent historical SMHM relation for the population's progenitors has a power-law form.

If we remove the assumption of a power-law growth history, we note that this ratio still describes the recent growth of the galaxies:

$$\frac{\text{SSFR}(t)}{\text{SMAR}(t)} = \frac{\frac{d\log M_*}{dt}}{\frac{d\log M_h}{dt}} = \frac{d\log M_*}{d\log M_h}, \tag{5}$$

which is valid as long as SSFR(t) and SMAR(t) are both positive. As shown in Figure (1), Equation (5) is really a geometric statement about the logarithmic SMHM plane. The SSFR sets the galaxies' velocity along the logarithmic stellar mass axis, and the SMAR sets the velocity along the logarithmic halo mass axis. The ratio of these two velocities ("rise over run") corresponds to the slope of the galaxies' trajectory in this plane; this slope will be constant as long as a power-law relationship between the galaxies stellar masses and halo masses holds (Equation (2)).

Equations (2) and (4) therefore yield a simple way to constrain galaxy progenitors. For this method, two galaxy stellar mass functions (SMFs) at nearby redshifts would suffice for observational constraints. The remaining inputs include host
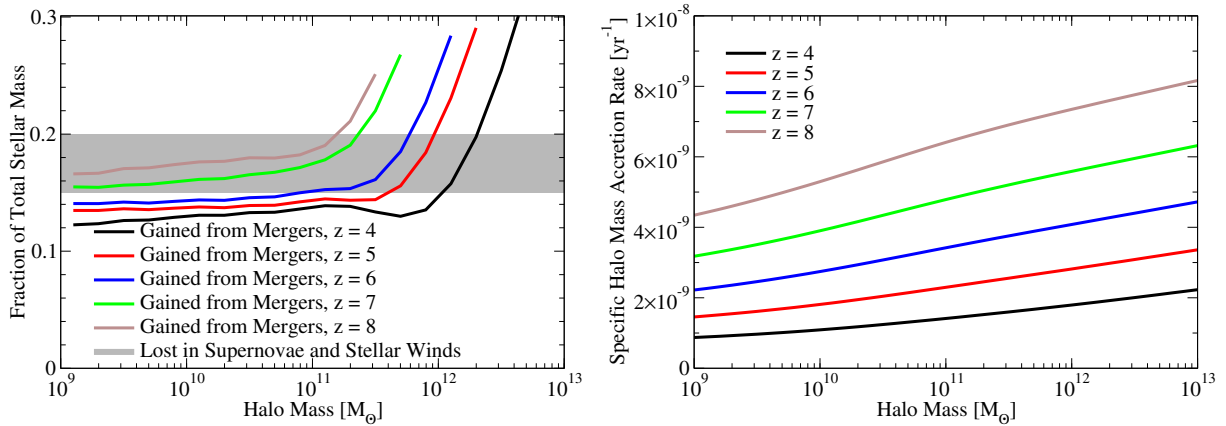
Figure 2. Systematic error considerations. Left panel: comparison of the stellar mass lost through supernovae and stellar winds with the stellar mass gained in mergers for galaxies at $4 < z < 8$, calculated from Behroozi et al. (2013c). In all cases, the stellar mass lost is very similar to the stellar mass gained. Right panel: average specific halo mass accretion rates, as a function of halo mass and redshift. The specific halo mass accretion rate depends only weakly on halo mass.

halo masses for the galaxies, which may be found by abundance matching/modeling (Section 3.2); halo mass accretion histories, determined via dark matter simulations (Section 3.3); and galaxy SSFRs, which are set by the growth of the SMF between the two redshifts (Sections 3.1 and 3.2). The ratio of the galaxies' SSFRs to their host halos' specific halo mass accretion rates (Equation (4)) then yields the power-law slope of the progenitors' historical SMHM relation. This can be used to infer basic information about the galaxies' progenitors, including the progenitors' star formation histories, SSFRs, stellar masses, and halo masses. As no observations of the progenitors are required, this method can yield constraints on galaxy populations that are otherwise too faint or at too high of a redshift to be observed directly.

We note in passing that Equation (5) applies for any pair of coupled variables. For example, one may also model the growth of black holes in galaxies using the ratio of specific black hole mass accretion rates to SSFRs. Current research in the coevolution of black holes in galaxies has focused on the correlation between black hole accretion rates and SFRs (see, e.g., Silverman et al. 2008; Aird et al. 2010; Mullaney et al. 2012; Conroy & White 2013; Chen et al. 2013; Hickox et al. 2014). Considering the relationship between the specific rates instead may be an interesting avenue for future research.

2.2. Stellar Mass Loss, Mergers, Scatter, and the Initial Mass Function

A galaxy's stellar mass can change not only because of new star formation (Equation (1)) but also through stellar mass loss (stellar winds and supernovae) and mergers of smaller galaxies. We adopt the stellar mass loss fraction as a function of time from Behroozi et al. (2013c), which is based on the flexible stellar population synthesis (FSPS) model (Conroy et al. 2009; Conroy & Gunn 2010) and the initial mass function (IMF) of Chabrier (2003):

$$f_{\text{loss}}(t) = 0.05 \ln\left(1 + \frac{t}{1.4\,\text{Myr}}\right). \quad (6)$$

The logarithmic form results in a very rapid 15% loss over the first 25 Myr, followed by another more gradual loss of 15% over the next 500 Myr. For the high-redshift ($z > 4$) galaxies we consider, typical SSFRs are on the order of 5–$10 \times 10^{-9}\,\text{yr}^{-1}$ (Behroozi et al. 2013c), which leads to characteristic formation timescales of 100–200 Myr. Since these timescales fall in the gradual loss regime, the overall stellar mass

loss is quite insensitive to the exact star formation histories and is in the range 15%–20%.

We next calculate the expected gain in stellar mass from mergers. This is a convolution between halo merger rates and the SMHM relation, both of which we take from constraints in Behroozi et al. (2013c). As shown in the left panel of Figure 2, merging halos contribute about 12%–18% of the total stellar mass in most galaxies for $4 < z < 8$; very massive galaxies may receive up to a 30% contribution. This small fraction can be understood from the fact that the SMHM ratio declines with halo mass, so most of the incoming stellar mass will come from major mergers (Behroozi et al. 2014b). The aforementioned star formation timescales ($\sim 150\,\text{Myr}$) are shorter than the expected major merger timescales (~ 1 per 300 Myr from $z = 8$ to $z = 6$; Fakhouri & Ma 2008; Fakhouri et al. 2010; Behroozi et al. 2013c), meaning that mergers contribute a minority of the stellar mass growth.

As a result, mergers and stellar mass loss nearly cancel each other's effects (Figure 2, left panel), representing only a 5%–10% total correction to α in Equation (4). From $z = 8$ to $z = 4$, halos grow by a factor of ~ 1 dex, so this correction would result in a 0.1–0.2 dex error in the inferred stellar masses over this range (see also Equation (7)). This is well within typical 0.3 dex systematic errors for stellar masses (Conroy et al. 2009; Behroozi et al. 2010, 2013c). All the same, we correct the stellar mass in Equation (4) to remove stellar mass from mergers and to include stellar mass lost as a result of passive evolution. This process is described in Section 3.2.

Another potential source of error is scatter in halo mass at fixed stellar mass. The average specific halo mass accretion rate is an extremely weak function of halo mass (Figure 2, right panel). For example, a change of ± 0.3 dex in halo mass corresponds to a change of $\pm 5.5\%$ in the SMAR for $10^{12}\,M_\odot$ halos. However, galaxy mass may correlate with a halo's recent accretion rate, which can bias the galaxies' host halo specific accretion rates. We avoid these kinds of selection biases by directly constraining the average stellar mass and the average SFR as a function of halo mass (as in Behroozi et al. 2013c), as discussed in Section 3.2. This allows us to select galaxies at fixed halo mass; the corresponding average specific halo mass accretion rates can then be calculated in an unbiased way from a dark matter simulation (Section 3.3 and Figure 2, right panel).

Finally, the choice of IMF has a minimal effect. The primary effect of switching, e.g., to a Salpeter (1955) IMF would be to identically rescale the SFR and stellar mass, leaving their
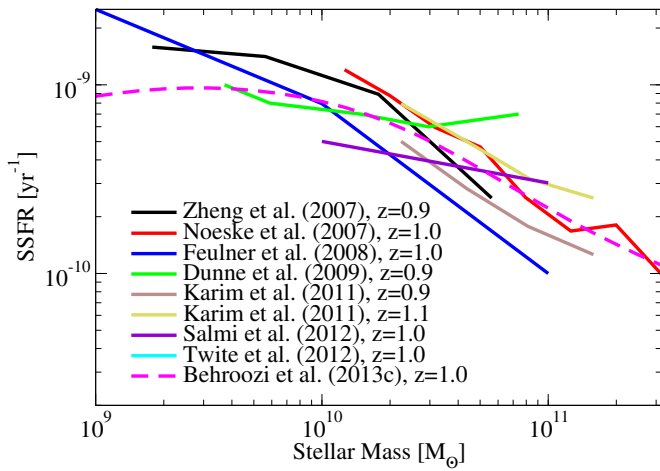
Figure 3. Directly measured SSFRs at $0.9 < z < 1.1$ from recent literature (Zheng et al. 2007; Noeske et al. 2007; Feulner et al. 2008; Dunne et al. 2009; Karim et al. 2011; Salmi et al. 2012; Twite et al. 2012) show significant scatter in both amplitudes and slopes. Except where specified, we adopt the SSFRs from the meta-analysis technique in Behroozi et al. (2013c), which incorporates these and other published constraints on galaxy SSFRs, as well as constraints from the growth of the SMF from $z = 8$ to $z = 0$.

ratio unchanged (Conroy et al. 2009). Although the stellar mass normalization would be affected, the predicted evolution (from Equation (4)) would remain the same. A secondary effect would be to change the inferred stellar mass loss by 5%–10%, depending on galaxy metallicity (Shimizu & Inoue 2013), but this would not change the ratio of the SFR to the total stellar mass ever formed, which is what is relevant for Equation (4). However, we note the possibility that the IMF may change to be more top-heavy at high redshifts for reasons including lower metallicities, high gas opacity, ultracompact star clusters, tidal shear, or rising cosmic microwave background temperatures (see Scalo 2005; Bonnell et al. 2007 for reviews). Some specific recent examples are given for starbursts in Weidner et al. (2011), for low metallicity at high redshift in Narayanan & Davé (2013), for ultracompact star clusters and low metallicity in Marks et al. (2012), and for disturbed galaxies in Habergham et al. (2010).

3. CONSTRAINTS FROM OBSERVATIONS AND SIMULATIONS

We discuss direct SSFR measurements in Section 3.1, our method for constraining stellar masses and SSFRs as a function of halo mass and redshift in Section 3.2, and the dark matter simulations we use in Section 3.3.

3.1. Measuring Specific Star Formation Rates

SSFRs are difficult to measure directly. This is clearest at low redshifts, where many independent determinations are available; e.g., Figure 3 compares several direct measurements of the $z = 1$ SSFR from recent literature. These have all been normalized to a Chabrier (2003) IMF; however, significant disagreement is present in both the amplitudes and slopes of the measurements. Behroozi et al. (2013c) found that this level of scatter (± 0.3 dex) between different publications' direct measurements is present at all redshifts—even for those now considered nearby ($z < 0.5$).

The magnitude of these uncertainties is important because they directly translate into the uncertainty in the power-law slope of the star formation efficiency inferred from Equation (4) (see Section 4). For that reason, it is not appropriate to rely on

SSFR measurements from a single source. We instead rely on the meta-analysis technique described in Behroozi et al. (2013c) and Section 3.2, which combines constraints from many different direct SSFR measurements with constraints from the growth rate of the SMF. For our methodology tests (Section 4), we restrict the meta-analysis to data obtained at $z \leqslant 5$; for our predictions (Section 5), we use the full data for $z \leqslant 8$.

As shown in Figure 3, this meta-analysis process is largely equivalent to taking the median of the published direct SSFR measurements. However, for completeness, we discuss the results from using single-source direct measurements of the SSFR in Appendix A.

3.2. Constraining the Stellar Mass–Halo Mass Relation and Specific Star Formation Rates through Abundance Modeling

We here distinguish abundance *modeling* from abundance *matching*. The latter nonparametrically constrains the SMHM relation by assigning galaxies ranked by decreasing stellar mass to halos ranked by decreasing halo mass within equal volumes. Abundance modeling instead assumes a parametric form (usually informed by abundance matching) for the SMHM relation and uses a Markov Chain Monte Carlo (MCMC) method to constrain the posterior distribution for the SMHM parameters. This approach benefits because observational constraints besides the SMF at a single redshift may be readily incorporated into the MCMC likelihood function. Examples include SMFs at multiple redshifts (Moster et al. 2010, 2013; Behroozi et al. 2010, 2013c; Yang et al. 2012; Béthermin et al. 2012; Wang et al. 2013; Lu et al. 2014), SFRs (Behroozi et al. 2013c), correlation functions (Yang et al. 2012; Leauthaud et al. 2012; Tinker et al. 2013), conditional SMFs (Yang et al. 2012; Lu et al. 2014), and weak-lensing constraints (Leauthaud et al. 2012; Tinker et al. 2013). The ability to include systematic uncertainties and covariances in the likelihood function is also advantageous (Behroozi et al. 2010, 2013c; Yang et al. 2012).

We follow the same technique used in Behroozi et al. (2013c), and we refer readers to that paper for full details. Briefly, we adopt a six-parameter functional form to describe the SMHM relation at a single redshift. This form includes parameters for a characteristic halo mass and stellar mass, a faint-end power-law slope, a massive-end turnoff, a shape for the transition between faint- and massive-end behavior, and the scatter in stellar mass at fixed halo mass. For each parameter, three variables control the evolution at low ($z < 0.5$), medium ($0.5 < z < 2$) and high ($z > 2$), redshifts, giving a total of 18 variables to describe the evolution of the SMHM relation. We additionally include nuisance parameters for systematic effects, including systematic offsets in recovered stellar masses for active and passive galaxies, random errors in stellar masses, incompleteness at high redshifts due to dusty and/or bursty star formation, and the fraction of stellar growth due to in situ star formation versus ex situ mergers.

Every location in this parameter space corresponds to a specific choice for the SMHM relation, $SM(M_h, z)$, as a function of halo mass and redshift. For the halo mass definition, we use the peak historical virial (Bryan & Norman 1998) halo mass along halos' growth trajectories (M_{peak}), which was found by Reddick et al. (2013) to be the best halo mass proxy for reproducing galaxy clustering and luminosity functions. Each choice of $SM(M_h, z)$ then represents a unique way to assign stellar masses for every halo at every time step in a dark matter simulation. The expected SMF at any redshift is therefore set by the number density of galaxies in dark matter halos; expected

SSFRs and CSFRs are set by the growth of galaxies along dark matter merger trees. The closeness of these expectations to observed constraints gives the relative likelihood for the chosen parameter set; an MCMC algorithm then determines the posterior distribution of allowable SMHM relations, as well as the implied SSFRs as a function of halo mass and redshift (required by Sections 2.2 and 3.1). As the dark matter halo merger trees allow full bookkeeping for the amount of stellar mass accreted in mergers and lost through passive stellar evolution, these corrections to galaxy stellar masses can be readily subtracted, as discussed in Section 2.2.

For observational constraints, we use the compilation in Behroozi et al. (2013c). This includes SMFs (Baldry et al. 2008; Pérez-González et al. 2008; Marchesini et al. 2009, 2010; Stark et al. 2009; Mortlock et al. 2011; Lee et al. 2012; Bouwens et al. 2011; Bradley et al. 2012; Moustakas et al. 2013), SSFRs (Yoshida et al. 2006; Salim et al. 2007; Zheng et al. 2007; Smolčić et al. 2009; Shim et al. 2009; Le Borgne et al. 2009; Dunne et al. 2009; van der Burg et al. 2010; Kajisawa et al. 2010; Ly et al. 2011a, 2011b; Rujopakarn et al. 2010; Cucciati et al. 2012; Robotham & Driver 2011; Tadaki et al. 2011; Magnelli et al. 2011; Karim et al. 2011; Bouwens et al. 2012a; Sobral et al. 2013), and CSFRs (Salim et al. 2007; Noeske et al. 2007; Zheng et al. 2007; Daddi et al. 2007; Feulner et al. 2008; Kajisawa et al. 2010; Schaerer & de Barros 2010; Lee et al. 2011; Tadaki et al. 2011; Karim et al. 2011; McLure et al. 2011; González et al. 2014; Reddy et al. 2012; Twite et al. 2012; Whitaker et al. 2012; Salmi et al. 2012; Labbé et al. 2013) from $z = 8$ to $z = 0$. For the tests in Section 4, we have also performed a restricted analysis excluding all verification data—i.e., all data at $z > 5$.

The main output of this model is the posterior distribution for $M_*(M_h, z)$—i.e., the stellar mass as a function of halo mass and redshift. As averaged SFRs as a function of halo mass and redshift are available from the intermediate steps in the calculation, we can straightforwardly calculate the posterior distribution of SSFRs as a function of redshift and halo mass.

3.3. Dark Matter Simulations and Halo Mass Accretion Rates

Halo properties are derived primarily from the *Bolshoi* simulation (Klypin et al. 2011). Bolshoi follows 2048^3 (8.6×10^9) dark matter particles in a 250 Mpc h^{-1} comoving, periodic box from $z = 80$ to $z = 0$ using the ART code (Kravtsov et al. 1997; Kravtsov & Klypin 1999). Its mass and force resolution ($1.9 \times 10^8 M_\odot$ and 1 kpc h^{-1}, respectively) allow it to resolve dark matter halos down to $10^{10} M_\odot$. The assumed cosmology is a flat, ΛCDM cosmology with parameters $\Omega_m = 0.27$, $\Omega_\Lambda = 0.73$, $h = 0.7$, $\sigma_8 = 0.82$, and $n_s = 0.95$; these are very close to the *WMAP9*+BAO+H_0 best-fit values (Bennett et al. 2013). Dark matter halos were found using the ROCKSTAR phase-space temporal halo finder (Behroozi et al. 2013d); merger trees were assembled using the CONSISTENT TREES code (Behroozi et al. 2013e), which reconstructs missing halos in merger trees to preserve gravitational consistency across simulation time steps.

As discussed in Sections 2.1 and 3.2, our approach requires the average growth rate, $\langle \dot{M}_{\mathrm{peak}} \rangle$, for halos as a function of redshift and mass. Behroozi et al. (2013c) already determined the *median* mass accretion histories for halos in Bolshoi; we therefore build on this existing fit, which is expressed as a function of the $z = 0$ halo mass and the scale factor. The full calibration and fitting procedure are discussed in Appendix B. For the halo mass function, we adopt the modified Tinker et al. (2008) form in Behroozi et al. (2013c), which was fit to the Bolshoi halo mass function for $0 < z < 8$.

Bolshoi's constraints on halos weaken above $z = 8$, due to its mass completeness limit. However, extrapolating the Behroozi et al. (2013c) halo mass function fit to higher redshifts compares well to the fit in Watson et al. (2013), which is calibrated to $z = 26$. We find maximum differences of 15%–25% between the two mass functions from $z = 10$ to $z = 15$; these are consistent with systematic biases from the choice of halo finder (Knebe et al. 2011, 2013; Watson et al. 2013). We also have compared to the average mass accretion histories in Wu et al. (2013), finding a maximum difference of 5% in the SMARs at $z > 10$.

4. TESTS AND ERROR ANALYSES

4.1. The Stellar Mass–Halo Mass Relation

In this section, we check how well Equations (2)–(4) can be used to derive the $z > 4$ SMHM relation from the $z = 4$ galaxy SMHM relation, SSFRs, and halo SMARs. Starting at $z = 4$ is motivated because we approximated galaxies' historical SMHM relationships as pure power laws (Equation (2)). This approximation is most appropriate if the galaxy's history is dominated by a single feedback mode (e.g., stellar feedback) for star formation (see Section 2.1); at $z \leqslant 4$, AGN-mode or other feedback in massive galaxies results in rapidly declining star formation histories (Behroozi et al. 2013c).[6] Note that while any starting redshift $z \geqslant 4$ is reasonable, we choose $z = 4$ because it gives the longest redshift baseline ($\Delta z = 4$ for galaxies up to $z = 8$) over which we can test the predictions of Equations (2)–(4).

Predicting the high-redshift SMHM relation is only a fair test if no high-redshift data has been used as a constraint. To that end, we have rerun the abundance modeling framework discussed in Section 3.2 using observational data constraints covering $0 < z \leqslant 5$. As noted in Sections 3.1 and 3.2, the inclusion of SMF data at $z = 5$ allows the growth of the SMF to serve as a constraint on galaxies' SSFRs at $z = 4$. The resulting best-fit SMHM relation and SSFRs at $z = 4$ are shown in comparison to the results of (Behroozi et al. 2013c; which used data constraints from $0 < z \leqslant 8$) in the top panels of Figure 4. The best-fitting SMHM relation of the restricted analysis is (as expected) slightly different from the best-fitting result of Behroozi et al. (2013c), but it is still well within the observational error bars.

The quantitative predictions from assuming that galaxies' ratios of SSFRs to halo SMARs remain constant (Equation (4)) over $5 \leqslant z \leqslant 8$ are shown in the middle and lower panels of Figure 4. These predictions are extremely consistent with constraints on the evolution of the SMHM relationship to the highest available redshift ($z = 8$) from Behroozi et al. (2013c). They are also consistent with nonparametric abundance matching of SMFs at those redshifts (Figure 4), within the expected systematic observational errors. While the shape and amplitude of the SMHM relation remain relatively constant, the halo mass corresponding to peak integrated star formation efficiency evolves from $\sim 10^{12} M_\odot$ at $z = 4$ to $\sim 10^{11} M_\odot$ at $z = 8$.

For $z = 4$ galaxies, the ratio of their SSFRs to their SMARs is fairly close to unity: $\alpha \sim 1$–1.5 (Figure 4, top right panel). If the SSFRs and SMARs were equal ($\alpha = 1$), the relative growth rates of galaxy stellar mass and host halo mass are the same—so

---

[6] As discussed in Appendix A, Equations (2)–(4) still give correct results for galaxies with more complicated histories, although only for the galaxies' recent past.
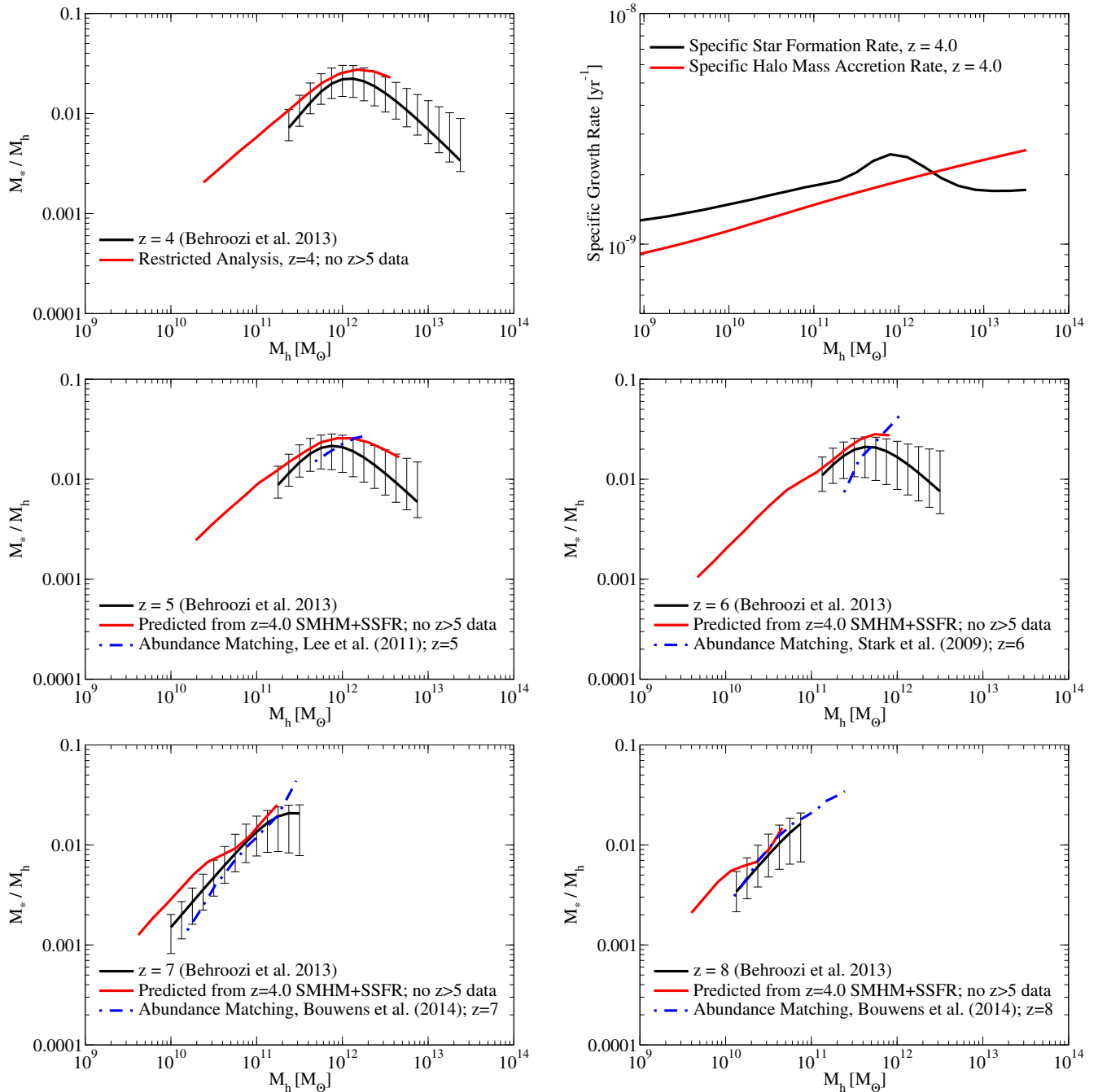
Figure 4. Tests of the method in Section 2 for predicting high-redshift SMHM ratios. Top panels: inputs for predicting galaxy evolution (Equation (4)). These include the SMHM ratio (top left panel), the SSFR (top right panel), and the specific halo mass accretion rate (top right panel) at $z = 4$. The SMHM ratio and SSFRs were derived from the method in Section 3.2, excluding all observational constraints at $z > 5$. Middle and bottom panels: predictions from Equations (2) and (4), compared to constraints from Behroozi et al. (2013c). Error bars in the Behroozi et al. (2013c) results represent 68% confidence intervals, and are largely dominated by observational systematics. The blue lines show nonparametric abundance matching results for $z = 5$ to $z = 8$, assuming zero scatter between stellar mass and halo mass; the SMFs used at each redshift are denoted in the figure legends. For the highest redshifts, SMFs were derived from Bouwens et al. (2014c) luminosity functions using the conversion in González et al. (2011); see Behroozi et al. (2013c) for full details.

that the historical SMHM *ratio* remains constant. For α slightly greater than unity, this will still be approximately true, so that the historical SMHM ratios will have at most a weak dependence on their historical halo mass. So, the galaxies forming stars at peak efficiency at $z > 4$ will be the progenitors of the galaxies forming stars at peak efficiency at $z = 4$. Similarly, the halo mass at which the SMHM ratio reaches any chosen amplitude is also expected to evolve (see also Section 5.2).

The uncertainties in these predictions grow as the redshift baseline increases. At high redshifts, halo growth is very

nearly exponential with redshift (Wechsler et al. 2002; McBride et al. 2009; Wu et al. 2013; Behroozi et al. 2013c); we find from the simulations in Section 3.3 that dM_h/dz is 0.25 dex. From Equation (4), the errors in stellar mass predictions then increase as

$$\Delta M_* \approx -0.25\epsilon\alpha\Delta z \text{ dex}, \qquad (7)$$

where $\alpha \sim 1$ is the ratio of SSFRs to SMARs (see, e.g., Figure 4), and ϵ is the fractional uncertainty in α. The predicted evolution and the fully constrained evolution over $z = 4$ to
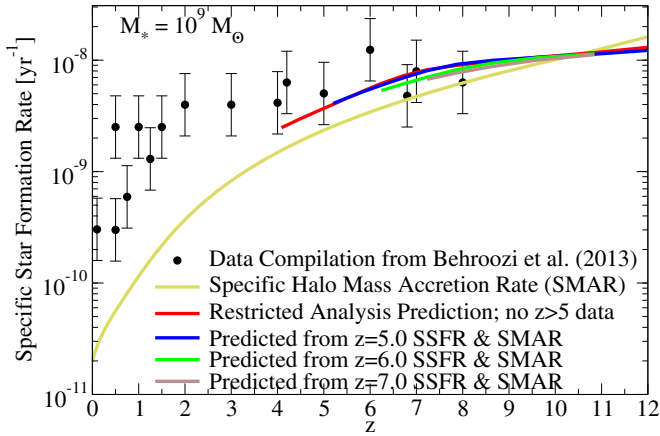
Figure 5. Observed SSFRs for $10^9 \, M_\odot$ galaxies compared to the SMARs (SMARs) of their host halos; corrections for nebular emission lines are included. See similar figure in Weinmann et al. (2011). A high SSFR to SMAR ratio (e.g., at $z < 2$) means that the fraction of incoming baryons converted into stars is currently much higher than it was for the galaxies' progenitors (see Section 2). A ratio near unity (e.g., at $z > 4$) means that the baryon conversion fraction has not increased as significantly. Also shown are extrapolations of SSFRs to $z = 12$ from Equation (4), calculated from the SSFR to SMAR ratio at $z = 4$, 5, 6, or 7, respectively (see Sections 4 and 5.1). The lack of $10^9 \, M_\odot$ galaxies at $z > 12$ prevents further extrapolation from being useful.

Figure 6. Comparison of observed CSFRs (data sources from Behroozi et al. 2013c) to extrapolations of CSFRs to $z \sim 15$ from Equation (4), assuming that the ratio of the SSFR to the SMAR is fixed to its value at $z = 4$, 5, 6, or 7, respectively (see text). Predicted observations assume a UV luminosity threshold of $M_{1500,AB} < -18$ for detecting individual galaxies.

$z = 8$ typically differ by 0.25 dex or less (Figure 4), which implies that ϵ is ~25% or less.

4.2. Specific and Cosmic Star Formation Rates

We next calculate how Equation (4) predicts that the SSFR for $10^9 \, M_\odot$ galaxies changes with redshift (Figure 5), given SSFRs and SMARs at $z = 4$ (Figure 4). At fixed redshift, more massive galaxies have lower SSFRs and larger specific halo mass accretion rates (SMARs) than smaller galaxies (see, e.g., Figure 4). As a result, they would be expected to maintain a smaller SSFR–SMAR ratio over their growth history (Equation (4)). The more massive the galaxy is at $z = 4$, the higher the redshift when it reached $10^9 \, M_\odot$. Since more massive galaxies have lower SSFR–SMAR ratios (Figure 4), we expect that the SSFR–SMAR ratio at fixed stellar mass will decline with increasing redshift.

This is exactly what is shown in Figure 5. While the SMAR rises steadily with redshift, the declining SSFR–SMAR ratio leads to an apparent "plateau" (Weinmann et al. 2011), which is extremely consistent with the observed SSFRs at high redshifts.

We also show the expected observed CSFRs in Figure 6, again calculated from galaxy SSFRs at $z = 4$. To calculate these, we applied the expected SSFRs and the expected SMHM relationship (Section 4.1) to the halo mass function (Behroozi et al. 2013c). We integrated the resulting number density down to an assumed UV luminosity threshold of $M_{1500,AB} < -18$ (matching recent high-redshift observations; Oesch et al. 2014b), where UV luminosities were computed without including dust as described in Appendix C. As shown in Figure 6, the CSFRs expected from the SSFR to SMAR ratio of $z = 4$ galaxies are extremely consistent with existing observations from $z = 5$ to $z = 8$.

We note that the uncertainties on SSFRs are not as sensitive to the redshift baseline because the errors are not cumulative. The fractional uncertainty ϵ in the SSFR to SMAR ratio α translates directly into the fractional uncertainty in SSFRs. As $\epsilon \lesssim 25\%$ (Section 4.1), this suggests that SSFR predictions are extremely robust, as long as the assumption of a power-law
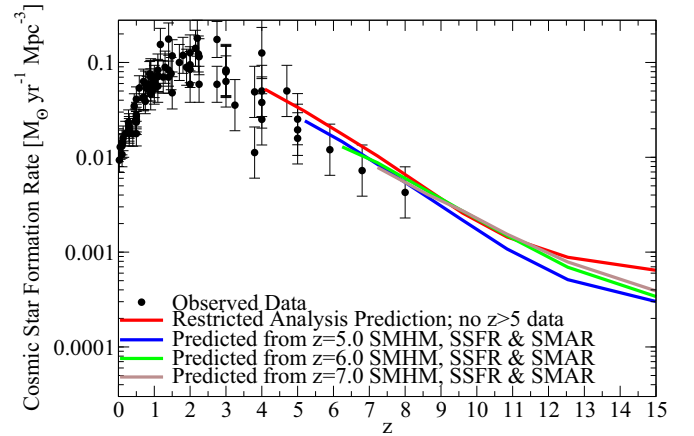
historical SMHM relation (Equation (2)) holds. Galaxy SFRs will be the product of the SSFR and stellar mass, which will result in fractional errors of

$$\frac{\Delta \text{SFR}}{\text{SFR}} = \log_{10}(1 + \epsilon) - 0.25 \epsilon \alpha \Delta z \text{ dex}. \quad (8)$$

Since the total integrated stellar mass must remain constant, an error in α will result in redistributing when past cosmic star formation happened. The error in Equation (8) thus has a sign change when $\log_{10}(1 + \epsilon) = 0.25 \epsilon \alpha \Delta z$. Noting that $\log_{10}(1 + \epsilon)$ is well approximated by $\epsilon \log_{10}(e)$ for small ϵ, this fractional error becomes zero for redshift baselines of $\Delta z = 4 \log_{10}(e) \alpha^{-1}$, regardless of what value ϵ actually takes! For typical values of α (~1.25), the total additional error from extrapolating the CSFR is minimized for a redshift baseline of $\Delta z = 1.2$.

5. RESULTS

We discuss predictions for high-redshift SSFRs and CSFRs in Section 5.1, stellar masses in Section 5.2, and sensitivity to errors in Section 5.3.

5.1. Predictions for Specific and Cosmic Star Formation Rates

As shown in Figure 5, we expect SSFRs to rise slowly with redshift at fixed galaxy mass. At $z = 4$ and above, galaxy SSFRs are nearly the same magnitude as host halo SMARs (see, e.g., Figure 4). As argued in Sections 2.1 and 4.1, the ratio of SSFRs to halo SMARs is conserved for progenitors of $z > 4$ galaxy populations; hence, higher-redshift SSFRs will also be about the same magnitude as the slowly rising halo SMARs. Since the choice of initial redshift is arbitrary, we show the SSFR evolution predicted from assuming constant SSFR-to-SMAR ratios for galaxies starting at $z = 5$, $z = 6$, and $z = 7$ in Figure 5. Consistent with the error analysis in Section 4.2, these predictions are all very similar to each other, as well as to the prediction from the restricted analysis in Section 4.2.

Predictions for observed CSFRs are shown in Figure 6; as in Section 4.2, we require galaxies to have a threshold UV luminosity of $M_{1500,AB} < -18$. These SFRs show a smooth decline from $z = 4$ to $z = 15$. As with SSFRs, we show predictions from assuming constant SSFR-to-SMAR ratios
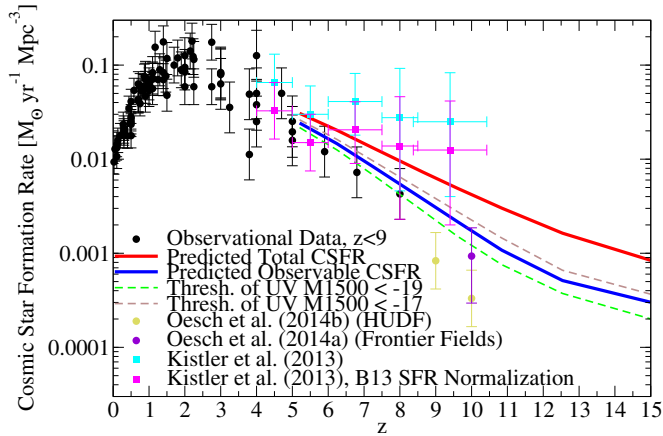
Figure 7. Comparison of our predictions (using galaxy SSFRs at $z = 5$) for high-redshift CSFRs with measurements from Oesch et al. (2014b) and Kistler et al. (2013). The red line shows the predicted total CSFR, and the blue line shows the predicted observed CSFR, which includes all galaxies with UV luminosities $M_{1500,AB} < -18$. The dashed lines show how the predictions would change if the threshold were changed to $M_{1500,AB} < -17$ or $M_{1500,AB} < -19$. Our predictions are systematically higher than the Oesch et al. (2014b) results by 1σ–2σ, although we are consistent with the Oesch et al. (2014a) results. Our predictions for the total CSFR agree well with Kistler et al. (2013), especially if their results are normalized to the $z = 4$ CSFR from the compilation in Behroozi et al. (2013c; purple points) instead of the older compilation in Hopkins & Beacom (2006; light cyan points).

(taken from Behroozi et al. 2013c) for galaxies starting at $z = 5$, $z = 6$, and $z = 7$, as well as from the restricted analysis in 4.2.

As noted in Section 1, Oesch et al. (2014b) found an apparent sharp steepening in the CSFR evolution beyond $z = 8$. In our model, we do not find this steepening to occur. Intuitively, this is because galaxy stellar mass doubling times at $z = 7$ and $z = 8$ are on the order of 100–200 Myr (see Figure 5). Hence, if galaxy SSFRs at $z = 7$ and $z = 8$ are correct, there should still be significant star formation ongoing at $z = 9$ and $z = 10$. If the Oesch et al. (2014b) results turn out to be correct, on the other hand, SSFRs at $z = 7$ and $z = 8$ would have to be a factor of three higher than current measurements (i.e., beyond existing corrections for nebular emission; Labbé et al. 2013). The tension between the Oesch et al. (2014b) measurements and our predictions is at the 1.5σ–2σ level (Figure 7). We find that the discrepancy is too large to be explained by cosmic variance uncertainties (Trenti & Stiavelli 2008), or by underestimating the effective UV luminosity threshold by a factor of 2.5 (Figure 7). Instead, these results may indicate that the UV–SFR conversion in Oesch et al. (2014b) underestimates the SFR for young stellar populations at lower metallicities (Castellano et al. 2014; Madau & Dickinson 2014). Alternately, the contamination exclusion criteria in Oesch et al. (2014b) may be too restrictive; e.g., removing point sources to exclude contamination from nearby stars may also affect compact galaxies at very high redshifts. We note that high-redshift measurements are rapidly evolving; as this manuscript was being revised, Oesch et al. (2014a) found a doubly imaged $z \sim 10$ candidate in the Frontier Fields, which may suggest a somewhat higher CSFR (Figure 7).

We can also predict the total (observed + unobserved) CSFR; galaxies too faint to be observed at a given redshift can be constrained by their descendants at a later redshift. A UV luminosity threshold of $M_{1500,AB} < -18$ is expected to miss nearly half of the total SFR at $z = 8$ and miss two-thirds by $z = 12$. Long gamma-ray bursts at high redshifts can also constrain

the total CSFR. Although significant calibration uncertainties remain for how the long gamma-ray burst rate depends on metallicity and redshift,[7] our predictions are generally within the 1σ error bars of current constraints (Kistler et al. 2009, 2013). We caution that Kistler et al. (2009, 2013) normalized the ratio of the cosmic gamma-ray burst rate to the CSFR using the CSFR calibration in Hopkins & Beacom (2006). As discussed in Behroozi et al. (2013c), more recent measurements of the CSFR have been systematically lower than the Hopkins & Beacom (2006) calibration by 0.3 dex; this new normalization would lower the GRB-derived SFRs by at least the same factor. As shown in Figure 7, lowering the Kistler et al. (2013) results by 0.3 dex results in excellent agreement with our predictions for the total CSFR.

5.2. Stellar Mass–Halo Mass Ratios

Given the ratios of galaxy SSFRs (from Behroozi et al. 2013c) to halo SMARs at $z = 4, 5, 6$, and 7 (from Section 3.3), we have used Equations (2)–(4) to predict SMHM ratios from $z = 9.6$ to $z = 15$ (Figure 8). As noted in Section 4.1, typical uncertainties in the stellar mass evolution are ~ 0.25 dex for a redshift baseline of $\Delta z = 4$ and ~ 0.5 dex for a redshift baseline of $\Delta z = 8$; these add in quadrature with existing 0.25 dex systematic uncertainties in the stellar mass normalization at $z > 4$ (Behroozi et al. 2013c; Curtis-Lake et al. 2013). We note that reionization may lead to non-power-law historical SMHM ratios for halo masses below $M_h = 10^9 M_\odot$ (Gnedin 2000; Noh & McQuinn 2014). However, several authors find that gas may cool in $10^8 M_\odot$ halos prior to reionization (Gnedin 2000; Noh & McQuinn 2014; Wise et al. 2014), so that predictions for $M_h < 10^9 M_\odot$ at very high redshifts (e.g., $z > 10$) may still be reasonable.

The median predicted evolution of the SMHM ratio is shown in Figure 9. We find that the redshift evolution seen in the SMHM ratio from $z = 4$ to $z = 8$ is expected to continue to very high redshifts. More quantitatively, we can calculate (as a function of redshift) the halo mass at which the stellar mass is 1% of the halo mass. The evolution of this halo mass with redshift is shown in Figure 10. At $z < 4$, this mass hardly evolves, which suggests that halo mass determines galaxy star formation efficiency at $z < 4$ (see also Behroozi et al. 2013b). At higher redshifts, this mass evolves continuously from $10^{11.5} M_\odot$ at $z = 4$ to $10^{9.3} M_\odot$ at $z = 15$—i.e., over two orders of magnitude across this redshift range. This evolution cannot be explained by appealing to an evolving halo mass definition. For example, it outpaces even that expected for constant v_{max} (the maximum of $\sqrt{GM(<R)/R}$ over the halo profile), which is a direct physical measure of the halo's potential well depth. The evolution at $z > 4$ may match better with a fixed central density (e.g., density within the central 1 kpc, as shown in Figure 10), which would correspond to a fixed cooling rate. However, galaxy formation is a complex process, and we cannot rule out contributions from other sources.

5.3. Sensitivity to Systematic Errors

5.3.1. Stellar Mass Functions

Results in this paper depend mostly on the growth of the SMF over redshifts from $z = 8$ to $z = 4$, especially since this growth largely constrains galaxy SSFRs (Section 3.2). We therefore address several uncertainties in high-redshift SMFs,

---

[7] Future work modeling the host galaxy demographics of long gamma-ray bursts (analogous to the short gamma-ray burst modeling in Behroozi et al. 2014a) will help improve existing uncertainties on the redshift and metallicity dependence.
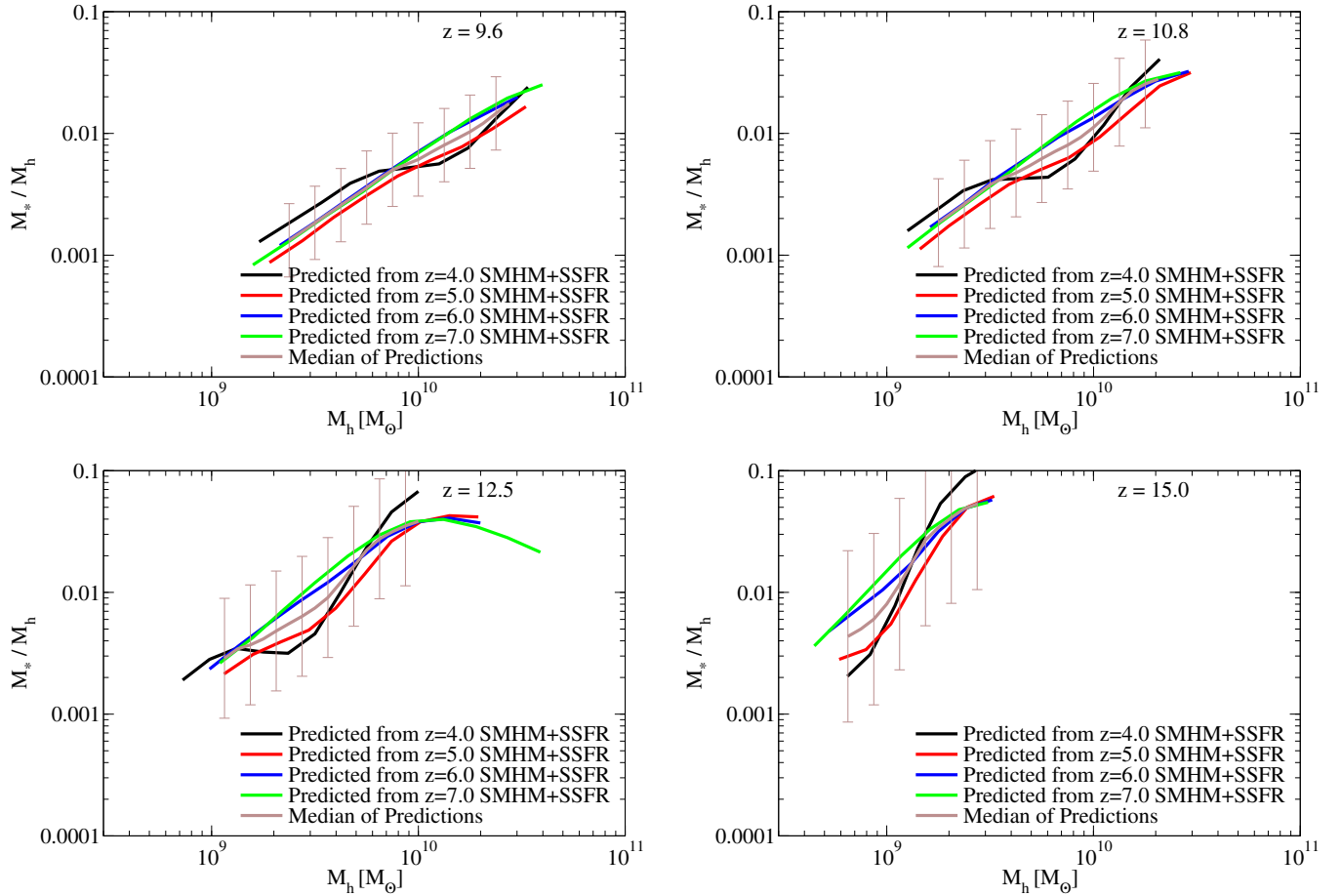
Figure 8. SMHM ratios for $z = 9.6$–15, predicted using Equations (2) and (4). The black, red, blue, and green lines show predicted evolution assuming that the ratio of galaxy SSFRs to halo SMARs is fixed at $z = 4, 5, 6$, and 7, respectively. The brown line shows the median of these predictions; the error bars give the expected 68% uncertainties on the prediction from the error analysis in Section 4.1.
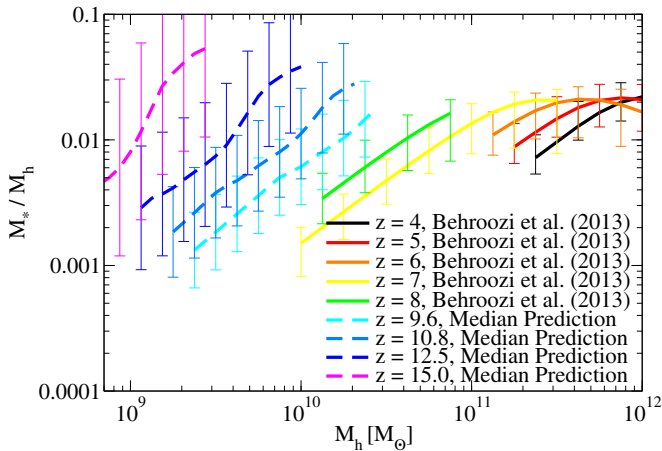

Figure 9. Evolution of median prediction for the SMHM ratio from Figure 8 for $z = 9$–15. Significant evolution in the efficiency at fixed halo mass is evident.

Figure 10. Evolution of the halo mass (M_h) at which the stellar mass (M_*) first reaches 1% of M_h. The black solid line shows the constraints from Behroozi et al. (2013c); the black dots show results from this work according to Figure 9. For comparison, lines of constant mass ($M_h = 10^{11.5} M_\odot$) and constant v_{max} ($v_{max} = 175$ km s^{-1}) are shown; these values are chosen to match the "1%" halo mass at $z = 4$. While the constant mass line describes the evolution reasonably well for $z < 4$, neither constant mass nor constant v_{max} tracks the mass evolution for $z > 4$. Instead, the evolution is much closer to the average mass accretion histories of halos, suggesting that high-redshift star formation efficiency may be more influenced by environmental factors (e.g., mass accretion rates) than at lower redshifts.

including ± 0.25 dex systematic biases in recovering stellar masses (Behroozi et al. 2013c; Curtis-Lake et al. 2013), sample variance from small survey volumes (± 0.1 dex for the $z > 7$ SMFs; Trenti & Stiavelli 2008), and low-redshift interlopers at the massive end of the SMF.

We cannot directly resolve interloper contamination, so we avoid presenting results from the bright end of the SMF, where such contamination is most an issue (e.g., galaxy stellar
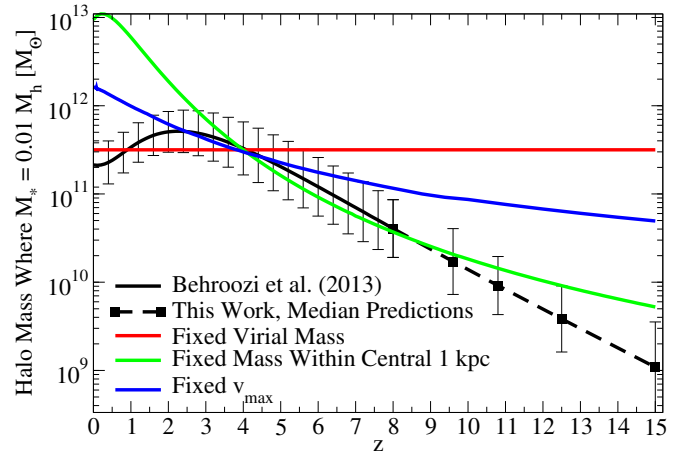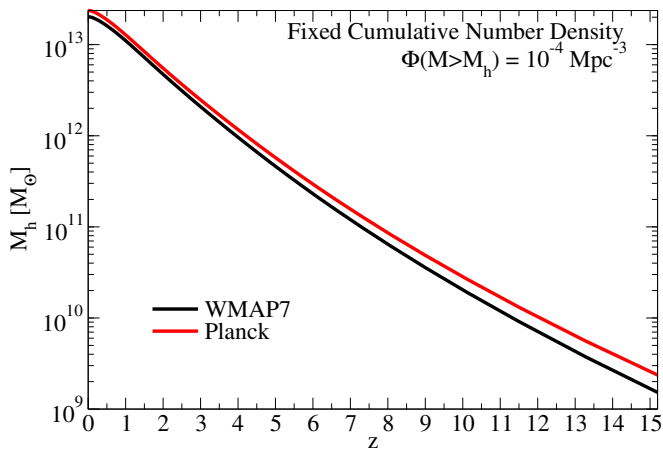
Figure 11. Halo masses at a fixed cumulative number density of 10^{-4} Mpc^{-3} for the *WMAP7* and Planck cosmologies, using the mass function fit from Behroozi et al. (2013c). Uniform systematic offsets in halo mass do not affect the main conclusions of this paper. The changes with redshift amount to a 0.01 dex (2%) difference in mass accretion rates (Appendix B). See Section 5.3.2 for discussion.

masses $> 10^{9.5} M_\odot$ at $z = 8$). The SSFRs we calculate as a function of halo mass are robust to the other two issues. Sample variance uncertainties are reduced because we use a smooth function to model the redshift evolution of the SMF (Section 3.2). Currently known uncertainties in computing stellar masses (e.g., assumed stellar population histories, dust modeling, uncertainties in stellar population synthesis) do not result in systematic biases that change rapidly with redshift or stellar mass. Therefore, when comparing two SMFs at two nearby redshifts, systematic biases will result in similar offsets to the stellar masses in both SMFs. The *relative* growth of stellar masses—i.e., SSFRs—computed from these SMFs will therefore be largely unaffected. While the absolute galaxy stellar masses will be affected by these biases, the inferred halo masses depend only on galaxy cumulative number densities as a function of stellar mass. So, as long as the systematic uncertainties do not destroy the overall rank ordering of galaxies (i.e., if there is a strong rank correlation between the true galaxy stellar masses and the observationally calculated galaxy stellar masses), the inferred halo masses will not be affected. As a result, the SSFRs as a function of *halo mass* are robust.

The systematic biases in absolute stellar masses do affect the SMHM relationships presented in this paper. We have included these uncertainties in the error bars in Figures 4, and 8–10; for high-redshift predictions, we have also included uncertainties from Equation (7). Yet, the conclusion that the characteristic halo mass for the SMHM relation changes from $z = 8$ to $z = 4$ is extremely robust to these uncertainties. As shown in Figures 9 and 10, the halo mass for a given SMHM ratio is significantly lower at $z = 8$ than it is at $z = 4$. Considering the slope of the SMHM relation, the stellar mass for a given halo mass is a full decade higher at $z = 8$ than it is at $z = 4$. This means that at fixed cumulative number density, galaxy stellar masses are 1 dex higher at $z = 8$ than would be predicted by keeping the $z = 8$ SMHM relationship the same as at $z = 4$. This level of evolution cannot be explained by known systematic biases, which are only of order ± 0.25 dex.

We note that the SMFs we have used for $z = 7$ and $z = 8$ were obtained by converting UV luminosity functions (Bouwens et al. 2014c) to SMFs using González et al. (2011). The González et al. (2011) conversion applied to luminosity functions at $z = 4$ and

$z = 5$ results in mass functions systematically too low compared to other results at $z = 4$ and $z = 5$ (e.g., Stark et al. 2009; Marchesini et al. 2010); however, it is in agreement with Stark et al. (2009) by $z = 6$. This may be because galaxies become systematically less dusty (Bouwens et al. 2014b) and younger (Figure 5) at high redshifts and so have higher luminosity-to-mass ratios. Nebular emission lines in high-redshift galaxies can bias stellar mass estimations (Stark et al. 2013; de Barros et al. 2014); however, using the González et al. (2011) conversion at $z \geqslant 6$ gives consistent results with these recent studies (D. Stark 2013, private communication). Owing to these concerns, we have generated UV luminosity functions from our assumed star formation histories and find that they agree directly with the Bouwens et al. (2014c) luminosity functions in Appendix C. Finally, we have checked that new SMFs from the CANDELS survey at $z > 6$ are within the error bars of the converted SMFs that we use (Duncan et al. 2014; Grazian et al. 2014).

5.3.2. Cosmology

The recent Planck cosmology results (Planck Collaboration et al. 2013) suggest that Ω_M may be higher and h may be lower than the values used in this paper (see, however, Spergel et al. 2013). We find that the differential comoving volume as a function of redshift (affecting SMFs and CSFRs) decreases by only 6%–7% for $z > 4$ when we adopt $\Omega_M = 0.307$ and $h = 0.68$. The increased Ω_M does result in an increase to the high-redshift halo mass function; at fixed cumulative number density, halo masses are ~ 0.08 dex larger at $z = 4$ and ~ 0.19 dex larger at $z = 15$ (Figure 11). This corresponds to an average change in mass accretion rates of 0.01 dex (2%), which we explicitly verify with halo merger trees in Appendix B.

A 2% change in halo mass accretion rates is within the existing uncertainties for the mass accretion rate fitting formula that we use (Appendix B); we therefore do not expect this to change predictions for SSFRs or CSFRs. The main effects on the SMHM relation would be systematic increases of 0.08–0.19 dex in halo masses at fixed galaxy mass. For the redshift range from $z = 4$ to $z = 8$, the ~ 1 dex change in characteristic halo mass (Figure 10) would be reduced by 0.04 dex if we had used the Planck cosmology. Naturally, uniform systematic offsets in halo masses do not affect our conclusions about the *evolution* of the characteristic halo mass.

6. DISCUSSION

As we have shown in Sections 2 and 4, the ratio of galaxies' SSFRs to their host halo SMARs sets the evolution of the galaxy progenitors' SMHM relations. Knowledge of two of these three quantities allows one to solve for the third, as discussed in Section 5. In this section we discuss several consequences of this three-way relationship, as well as implications of our predicted high-redshift galaxy evolution. We consider the SSFR "plateau" in Section 6.1, reionization in Section 6.2, expectations for *JWST* in Section 6.3, abundance matching in Section 6.4, and comparisons to other work in Section 6.5.

6.1. High-redshift Star Formation and the Changing Characteristic Mass Scale of Galaxy Formation

As shown in Figures 9 and 10, we find that the evolution of the SMHM relation can be very simply described. At $z < 4$, the SMHM ratio depends much more on halo mass than on redshift

(Behroozi et al. 2013b). At $z > 4$, however, the characteristic halo mass evolves strongly with redshift. More quantitatively, the halo mass at which M_* is 1% of M_h evolves as

$$M_{1\%} \sim \begin{cases} 10^{11.5} \, M_\odot & \text{if } z < 4 \\ 10^{11.5-0.23(z-4)} \, M_\odot & \text{if } z \geqslant 4 \end{cases}. \qquad (9)$$

This evolution at high redshift is close to the average accretion rate of halos (Figure 10), so the SMHM ratio is approximately unchanging as a function of cumulative number density or of peak height, ν.

As discussed in Section 5.3 and as shown in Figure 10, this mass evolution is much larger than can be explained by known systematic biases. We note not only that this mass evolution is consistent with flattening in SSFRs at high redshifts (Weinmann et al. 2011), but also that they are equivalent statements. For a galaxy population with a given stellar mass and redshift, the ratio of the galaxies' SSFRs to their host halos' SMARs is equal to the power-law slopes of their historical SMHM relations (Equations (2)–(4)). If these historical slopes are not completely parallel to the slope of the SMHM relation at the starting redshift, then galaxies will evolve off their original SMHM relationship—that is to say, the SMHM relationship as a whole must evolve with redshift. As a corollary, evolution in the ratio of galaxy SSFRs to their host halo specific halo mass accretion rates (e.g., Figure 5) *must* be accompanied by evolution in the SMHM relationship: as the ratio changes, the evolutionary trajectories of galaxies will change, and no single SMHM relationship can be parallel to all galaxy trajectories.

Flattening of galaxy SSFRs at high redshifts implies a decrease in the ratio of galaxy SSFRs to their host halo SMARs. In Figure 5, the ratio of galaxy SSFRs to host halo mass accretion rates is consistent (within observational errors) with the slope of the SMHM relation at fixed redshift, at least for $z < 4$. However, the ratio at higher redshifts is too low to be consistent. From Equation (5), if this ratio falls below the slope of the SMHM relationship at fixed redshift, and if the SMHM relationship has a positive slope, then the SMHM relationship will evolve to higher efficiencies at higher redshifts.

Hence, the growth rate of the SMF and the flattening in observed SSFRs both provide evidence that halos with masses below $10^{12} \, M_\odot$ formed stars more efficiently at very high redshifts than they did for $0 < z < 4$. Part of the reason for this may be a change in the gravitational potential well depth at fixed halo mass (Figure 10, Section 5.2). This is not likely the only explanation, as it would require evolution in the characteristic halo mass over $0 < z < 4$ (Figure 10); feedback efficiency at high redshift may also be reduced. However, other factors like increased central density at high redshifts (Figure 10) may decrease cooling times enough to explain the evolution.

6.2. Reionization

Knowing the cosmic star formation history, it is possible to calculate the hydrogen reionization history of the universe. We use the minimal reionization model of Haardt & Madau (2012):

$$\frac{dQ}{dt} = \frac{\dot{n}_{\text{ion}}}{n_{\text{H+He}}} - \frac{Q}{t_{\text{rec}}}, \qquad (10)$$

where Q is the reionized fraction, $\dot{n}_{\text{ion}}$ is the creation rate density of ionizing photons, $n_{\text{H+He}}$ is the number density of hydrogen and helium atoms, and t_{rec} is the recombination time. In this model, single ionization of helium is assumed to happen at the same time as hydrogen; we assume that the helium mass fraction is $Y = 0.24$. Ionizing photon production is given by

$$\dot{n}_{\text{ion}} = N_\gamma f_{\text{esc}} \text{CSFR}, \qquad (11)$$

where N_γ is the number of ionizing photons per unit mass of stars, f_{esc} is the average escape fraction from galaxies, and is the CSFR. For a low-metallicity Salpeter IMF, N_γ would be $5 \times 10^{60} \, M_\odot^{-1}$ (Alvarez et al. 2012). Since the Chabrier IMF that we use has fewer low-mass stars but the same number of high-mass (ionizing) stars, we take N_γ equal to $7.65 \times 10^{60} \, M_\odot^{-1}$; this corresponds to 6400 photons per baryon in stars. While inferences at $z < 5$ suggest escape fractions less than 10%, the escape fraction at high redshifts is very uncertain (Hayes et al. 2011). Simulations suggest that the escape fractions can be very large (Wise & Cen 2009; Wise et al. 2014); current models typically adopt either a constant f_{esc} or an f_{esc} that rises rapidly with redshift (Haardt & Madau 2012). In this paper we use a constant f_{esc} to simplify the interpretation of our results; we note that this would roughly correspond to the star-formation-weighted average f_{esc} for models in which f_{esc} evolves with time. To explore the range of uncertainties, we allow f_{esc} to vary from 0.1 to 0.6.

The recombination time is given by

$$t_{\text{rec}} = (\alpha_B n_{\text{H+He}} C)^{-1}, \qquad (12)$$

where we take α_B to be the case B recombination coefficient at 10,000 K for hydrogen (2.79×10^{-79} Mpc^3 yr^{-1}) and C to be the clumping factor. The determination of C is also uncertain, with estimates ranging from $C = 2$ to $C = 4$ at high redshifts (Haardt & Madau 2012); we take $C = 3$ as our fiducial value and allow C to vary from 2 to 4 for modeling uncertainties.

For any reionization history, we can also calculate an optical depth τ for Thomson scattering, given by

$$\tau = \sigma_T \int_0^{t_{\text{now}}} (Q n_{\text{H+He}} + Q_{\text{He III}} n_{\text{He}}) c \, dt, \qquad (13)$$

where σ_T is the Thomson cross section of an electron (6.986×10^{-74} Mpc^2), $Q_{\text{He III}}$ is the fraction of helium that has been doubly ionized, and n_{He} is the number density of helium. Since the double ionization of helium happens much later than single ionization, it changes τ by only $\sim$0.001; we therefore fix the redshift of double ionization to $z = 3.5$.

The largest uncertainty for τ is the escape fraction, followed by uncertainties in the normalization of the CSFR (Figure 12), followed by subdominant uncertainties in the clumping factor. If the CSFR at $z > 4$ were currently underestimated by a factor of two, an average escape fraction of 0.2 would be consistent with the most recent *Wilkinson Microwave Anisotropy Probe* (*WMAP*) results at the 1σ level. However, if current high-redshift CSFRs are correct, f_{esc} would need to average at least 0.5 during reionization. These escape fractions agree with other models that match the optical depth (e.g., Haardt & Madau 2012; Alvarez et al. 2012; Bouwens et al. 2012b; Robertson et al. 2013) and are plausible for certain types of galaxies (Wardlow et al. 2014; Dijkstra et al. 2014), but they are higher than typically seen in low-redshift observations (Hayes et al. 2011).

We also show the expected reionization history of the universe in Figure 13 for $f_{\text{esc}} = 0.5$. As with the optical depth, the normalization of the CSFR is a substantial uncertainty. For this escape fraction, 68% confidence limits on the redshift of half-reionization are $7 < z < 10$. Absent independent
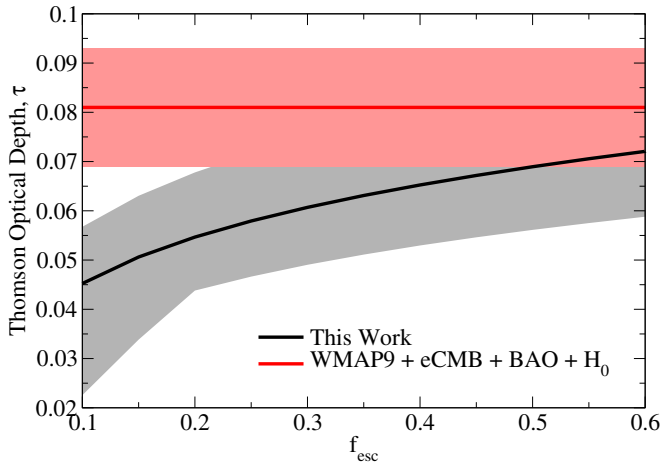
Figure 12. Optical depth as a function of ionizing photon escape fraction. The gray shaded region corresponds to the best-fit *WMAP9* 68% limits from Bennett et al. (2013). The red shaded region corresponds to 68% limits for our CSFR estimates. The errors come largely from ±0.3 dex systematic uncertainties in the total CSFR.
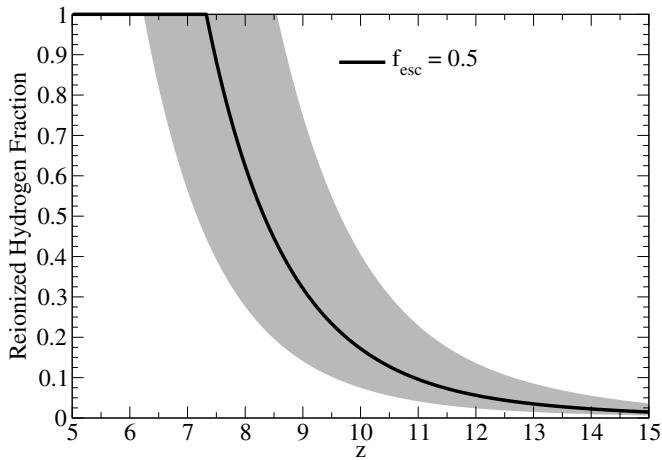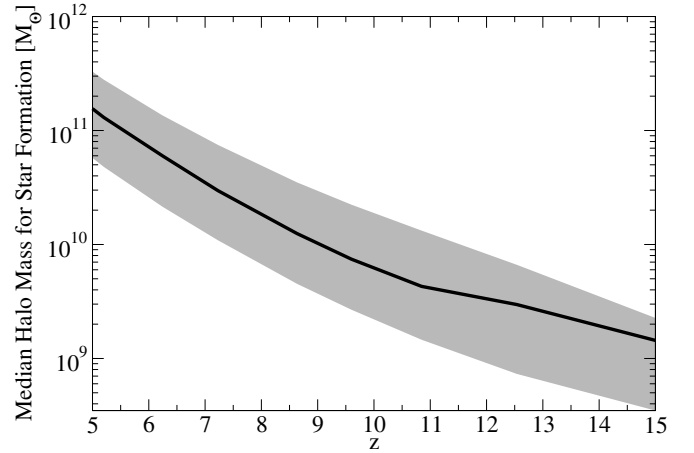

Figure 14 Halo mass below which 50% of star formation occurs as a function of redshift, i.e., the median halo mass for star formation. The errors are dominated by uncertainties on the faint-end slope of the SFR function.
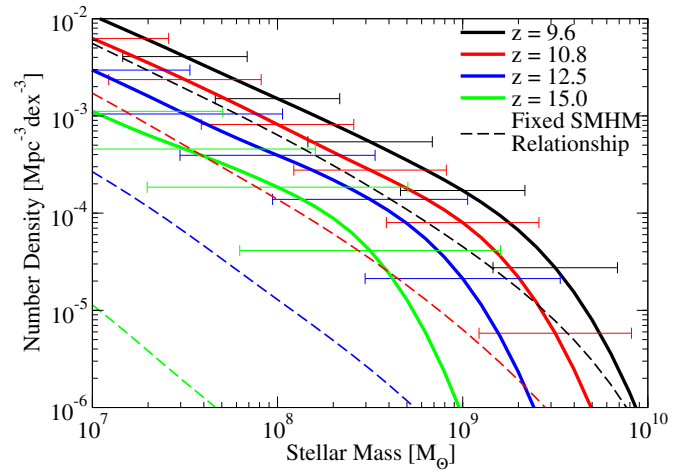

Figure 13 Reionization history of the universe assuming a star-formation-weighted average f_{esc} of 0.5. As with Figure 12, the 68% uncertainties (gray shaded region) come largely from systematic uncertainties in the CSFR.

Figure 15. Predictions for the evolution of the galaxy SMF to $z = 15$ (solid lines). Error bars show uncertainties in the evolution of stellar masses, from Equation (7). Dashed lines show how the SMFs would evolve if the SMHM relationship instead remained fixed to its $z = 8$ value. The latter case would result in over two orders of magnitude fewer galaxies observed by the *JWST* at $z = 15$.

constraints, the escape fraction is completely degenerate with the normalization of the cosmic star formation history in these models. This makes it difficult to use τ or the reionization history as a constraint on galaxy formation (or vice versa).

As noted in Alvarez et al. (2012) and Wise et al. (2014), an escape fraction that varies strongly with halo mass would result in an escape fraction that varies strongly with redshift (as assumed in Haardt & Madau 2012). This is because the median halo mass for star formation (i.e., the halo mass below which 50% of star formation occurs) is a strong function of redshift (Figure 14). From Figures 9 and 14, we expect that the galaxies that would reionize the universe at $z > 8$ are typically below $10^8\ M_\odot$ and their host halos are typically below $10^{10}\ M_\odot$. While escape fractions for these low-mass galaxies can be observed locally, we note that the nature of star formation in their high-redshift counterparts will likely be very different, as evidenced by the very different SMHM ratios (Figure 9).

6.3. Expectations for JWST

If low-mass halos continue to become more efficient at $z > 8$ (Figure 9), the *JWST* should be able to see many $M_* > 10^8\ M_\odot$

galaxies out to at least $z = 15$ (Figure 15; see also Appendix C for luminosity functions). By comparison, if the SMHM relation were fixed at $z = 8$ and did not evolve to $z = 15$, the expected number density of galaxies at $z = 15$ would drop by over two orders of magnitude (Figure 15). We expect that the *JWST* will rule out at least one of these two scenarios very shortly after launch. Owing to the rapid buildup of the halo mass function from $z = 15$ to $z = 8$, the number density of galaxies observed with the *JWST* will be very constraining for galaxy formation models.

We find that the expected faint-end slopes for the SMFs are -1.85 to -1.95 from $z = 9$ to $z = 15$. These are steep, suggesting that deeper *JWST* pointings will result in many more observed galaxies. However, none of the slopes are significantly steeper than the faint-end slopes we expect at $z = 8$ (-1.8), suggesting that the evolution in faint-end slopes observed over $4 < z < 8$ (Bouwens et al. 2012b) does not continue to higher redshifts.

We note that Equation (4) also constrains the *maximum* attainable SSFRs for galaxy populations as a function of

redshift. From Equation (4), we have

$$SSFR = \alpha SMAR. \qquad (14)$$

Hence, maximum SSFR would require maximizing the specific halo mass accretion rates (SMARs) and the power-law slope (α) of the historical SMHM relation. The maximum value of α is limited by available mechanisms to regulate star formation. For halos that are just large enough to accrete reionized gas ($\sim 10^9 \, M_\odot$; Gnedin 2000) and form their first stars, the SSFRs could be effectively infinite. At larger masses (e.g., $> 10^{10} \, M_\odot$), the most important mechanisms become stellar winds and supernovae from massive stars (Agertz et al. 2013). Typical values of α for $10^{10} \, M_\odot$ and larger halos range from $\alpha \approx 2$ at $z = 0$ to $\alpha \approx 1$ at $z > 4$. It is difficult to imagine that α could be much higher than two because the energy and momentum requirements for leaving a halo both scale as a low power of the halo mass. For example, the energy needed to escape from a halo scales as halo mass to the two-thirds power, and the escape velocity scales as halo mass to the one-third power. That said, we consider values from $\alpha = 1$ to $\alpha = 4$ to cover any exotic future feedback mechanisms.

Note that *all* variation from galaxy physics is contained in the slope α, and the range $\alpha = 1$ to $\alpha = 4$ constitutes only a ± 0.3 dex uncertainty in the maximum SSFRs for halos larger than $10^{10} \, M_\odot$. The uncertainty in specific halo mass accretion rates is negligible in comparison, as those are directly measurable from dark matter simulations (Appendix B). Hence, the maximum average SSFRs for a mass-selected galaxy population are limited to be within a factor of one to four of the SMARs at all redshifts, as shown in the top panel of Figure 16.

These constraints are consistent with existing measurements of galaxy SSFRs (Figure 16). They also place strong constraints on what typical stellar populations will look like at higher redshifts. For example, at $z = 10$, averaged SSFRs are limited to no more than $10^{-7.3} \, yr^{-1}$. If a survey returned higher average SSFRs for galaxies in a chosen stellar mass bin, it would most likely indicate that the survey was biased toward selecting highly star-forming galaxies, or that the analysis pipeline was giving biased stellar masses or SFRs.[8]

6.4. The "Too Big to Fail" Problem and Satellite Galaxy Abundance Matching

Redshift evolution in the SMHM relation at $z > 4$ can strongly affect the stellar mass for satellite galaxies. For example, the scatter in satellite stellar masses at fixed peak halo mass could be very large, depending on the distribution of satellite formation times. This is especially true for the satellite halo mass range expected to host the brightest dwarf satellites of the Milky Way ($\sim 10^9$–$10^{10} \, M_\odot$). Boylan-Kolchin et al. (2012) identified several Milky Way satellites that were much too bright compared to the $z = 0$ SMHM relation. Conversely, Boylan-Kolchin et al. (2012) found that not all of the most massive satellite halos of the Milky Way could host the brightest satellite galaxies (i.e., the "too big to fail" problem). While several papers have shown that the observations may be explained by a combination of cyclic feedback and tidal interactions with the disk of the Milky Way (Governato et al. 2012; Zolotov et al. 2012; Teyssier et al. 2013; Pontzen & Governato 2014), it remains possible that some of the satellites were formed and accreted very early in the history
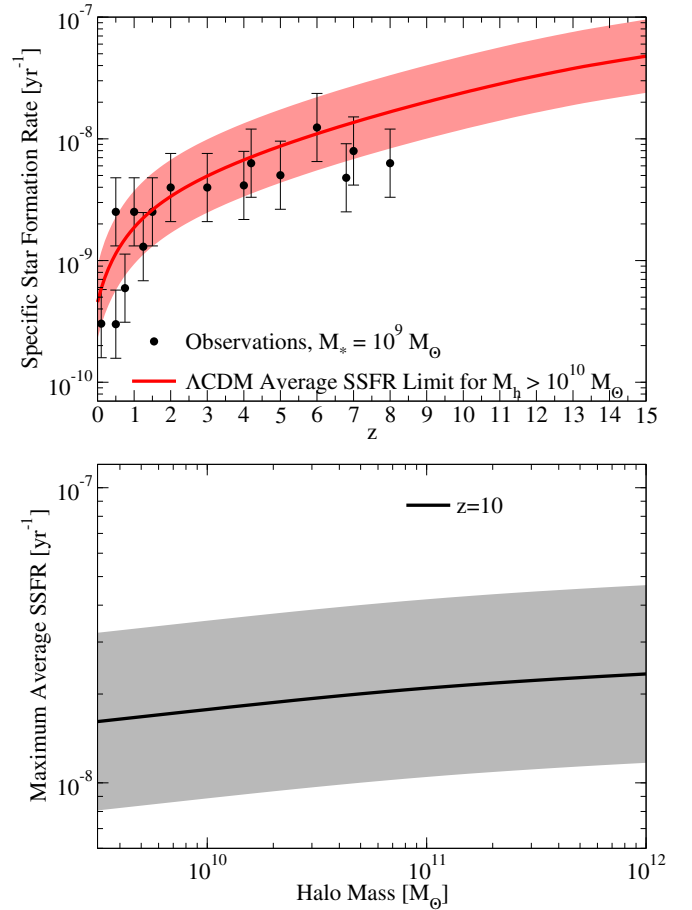

Figure 16 Top panel: maximum possible population-averaged SSFRs for galaxies with host halo masses $M_h > 10^{10} \, M_\odot$, as a function of redshift. Error bars show the allowable uncertainties from *all* unknown galaxy formation physics. Individual galaxies can temporarily exceed these limits, but the averaged population SSFRs are fundamentally limited by specific halo mass growth rates in ΛCDM (see Section 6.3). Bottom panel: maximum attainable averaged SSFRs at $z = 10$, as a function of host halo mass. Other redshifts also show a very weak dependence on halo mass.

of the universe. In this case, Figures 9 and 10 would suggest that these early-formed satellites should have a higher stellar mass than later-formed satellites at fixed circular velocity.

We briefly note that abundance matching methods typically match galaxies to halos using the SMHM relation at a single redshift. For satellites, this creates some consistency issues because it is often not clear whether it is better to use the SMHM relation at the time of the satellite's accretion or peak halo mass/peak maximum circular velocity (Behroozi et al. 2010; Yang et al. 2012; Moster et al. 2013). At $z < 2$, clustering and conditional luminosity functions indicate that satellite galaxy masses are best set by using the SMHM relation at a single redshift (Reddick et al. 2013; Watson & Conroy 2013); physically, this indicates continued star formation in a fraction of satellites after accretion (Wetzel et al. 2013). However, strong evolution in the SMHM relation at high redshifts suggests that abundance matching using the SMHM relationship at the time of accretion or peak halo properties will better capture satellite galaxy masses at $z > 4$.

6.5. Comparison with Previous Semiempirical Models

Several previous models, such as Trenti et al. (2010) and Wyithe et al. (2014), have assumed that high-redshift star

---

[8] Of course, it could also indicate that ΛCDM is wrong—though this avenue seems an unlikely way that this could be proven.

formation occurs in bursty episodes. Under this interpretation, many galaxies at $z > 4$ are unobserved because they are temporarily not forming stars. This assumption is in part based on rest-frame UV angular clustering measurements at $z > 4$, such as Lee et al. (2009). We note, however, that modeling angular clustering measurements can be extremely challenging. The Lee et al. (2009) conclusions are largely based on the discrepancy between the one-halo autocorrelation term of their model and the observed data. However, the one-halo term is dominated by satellites, which tend to have lower SFRs than central galaxies. As a result, the Lee et al. (2009) results largely constrain the duty cycle of *satellites*; if only 30% of satellites are star-forming at $z = 4$, this would still allow 90% of all galaxies to be star-forming, since the satellites make up a small fraction at these redshifts. Additional issues generic to all angular correlation functions are appropriately propagating uncertainties in the redshift distribution (which are difficult to determine for faint galaxies with UV-only detections) and understanding how the sample selection function (e.g., color–color cuts) affects the redshift-dependent average bias of the selected galaxies. We note that Conroy et al. (2006) finds no duty cycle to be necessary when matching angular correlation functions at $z = 4$ and $z = 5$, further suggesting that it is very difficult to use angular correlation functions as robust constraints on galaxy duty cycles.

Separately, Wyithe et al. (2014) argued for lower duty cycles so that the growth of the stellar mass density matches the CSFR; however, previous discrepancies have largely been resolved (Reddy & Steidel 2009; Bernardi et al. 2010; Moster et al. 2013; Behroozi et al. 2013c). Also, the concern in Wyithe et al. (2014) that $z > 4$ galaxies cannot have formed stars at their observed rates for an entire Hubble time is resolved by strong evidence for individual galaxies having rising SFRs (Papovich et al. 2011; Behroozi et al. 2013a, 2013c; Moster et al. 2013; Lee et al. 2014), as well as the overall rise in the total CSFR with time.

Because of problems with angular correlation functions, duty cycles at $z > 4$ may not be fully determined until future deep rest-frame optical observations (Wyithe et al. 2014). In our approach, we chose not to assume low duty cycles due to several heuristic arguments. Most importantly, UV light continues to be emitted by stellar populations up to 100 Myr old (Conroy et al. 2009; Castellano et al. 2014; Madau & Dickinson 2014). At $z = 8$, this is comparable to specific halo mass accretion rates—so even if a major starburst expels all the gas from a galaxy, an equal amount of replacement gas will have reaccreted by the time the first stellar population fades in the UV. At $z = 4$, halo SMARs are somewhat lower ($(2–3) \times 10^{-9}$ yr^{-1}), but the typical halo still grows by 20%–25% in 100 Myr. These high accretion rates make it difficult for stellar feedback to completely quench star formation on long timescales. Second, high quenched fractions at $z = 4$ are inconsistent with K-band-selected SMFs at $z < 4$ because they would imply a discontinuous jump between Lyman-break galaxy (LBG)-selected (at $z > 4$) and K-selected (at $z < 4$) SMFs. Instead, the growth of LBG-selected SMFs into K-selected mass functions is extremely consistent with measured SSFRs (Behroozi et al. 2013c; Moster et al. 2013).[9] Third, the quenched fractions measured in K-selected samples at $2 < z < 4$ are very low (Brammer et al. 2011; Muzzin et al. 2013) except at the very highest stellar masses, which is inconsistent with a large quenched fraction at

$z > 4$—unless the quenched galaxies at $z > 4$ all return to being star-forming at $z < 4$. Fourth, regardless of the feedback prescription, the observational duty cycle of galaxies above $10^9 M_\odot$ is unity in hydrodynamical simulations (G. Snyder & P. Hopkins, private communication; Jaacks et al. 2012b; Wise et al. 2014).

Despite the differences with our approach, both Trenti et al. (2010) and Wyithe et al. (2014) also find that galaxy star formation must be more efficient at high redshifts—in their language, that galaxies have higher duty cycles. Their conclusion is driven by the same evidence as ours, namely, that if the same SMHM or star formation–halo mass relationship for $z = 4$ halos were applied to $z = 8$ halos, the resulting stellar mass, SFR, and luminosity functions would be an order of magnitude less than observational constraints (Section 5.3.1). However, we note that the Trenti et al. (2010) extension to high redshifts ($z > 8$) is very different than ours because their duty cycle is nearly 100% at $z = 8$ and has no more room to grow. Hence, the Trenti et al. (2010) predictions are very similar to the case in Figure 15, where the SMHM relationship is assumed to be fixed for $z > 8$. As noted in Section 6.3, the *JWST* should be able to very quickly distinguish these two scenarios.

We note finally that Tacchella et al. (2013) took a very different approach, which was to model halo star formation histories as a combination of a burst and a longer-duration star formation mode. While this model provides an excellent match to luminosity functions, star formation histories of halos are not self-consistent across redshifts (S. Tacchella 2012, private communication). For example, the star formation history of $z = 5$ halos at $z > 6$ in the model is not consistent with the star formation histories of $z = 6$ halos at $z > 6$; so if applied to merger trees, the model would require retroactive modification of galaxy star formation histories. It is nonetheless still interesting mathematically to consider the resulting redshift evolution; the Tacchella et al. (2013) model also does not predict any break in the slope of the CSFR for $z > 8$.

7. CONCLUSIONS

We have presented a simple theoretical basis for predicting galaxy stellar mass, SSFR, and host halo mass evolution at high redshifts (Section 2.1). We reach the following conclusions.

1. The ratio of galaxies' SSFRs to their host halos' SMARs can be used to predict galaxies' evolution in the SMHM plane with redshift. (Sections 2.1, 4.1, and 4.2, Appendix A).

2. Tests of this predictive model with galaxy properties at $z = 4$ successfully match observational constraints on the SMHM relation, SSFRs, and CSFRs for $z = 5$–8 (Sections 4.1 and 4.2).

3. Galaxy SSFRs are expected to increase only mildly at higher redshifts (Section 5.1).

4. CSFRs are not expected to rapidly fall at $z > 8.5$, in contrast to recent *HST* measurements, but consistent with estimates from long gamma-ray burst rates (Section 5.1).

5. Halos smaller than $10^{12} M_\odot$ are expected to be increasingly efficient at star formation at $z > 4$ (Section 5.2), which is strongly linked with the "plateau" in galaxy SSFRs at fixed stellar mass (Section 6.1).

6. This evolution in efficiency is too strong to allow star formation efficiency to be set only by gravitational potential well depth at $z > 4$ (Section 5.2); at $z > 4$, halos maintain similar SMHM ratios along their progenitor histories.

---

[9] This argument also excludes dust from hiding many galaxies at $z > 4$.

7. Matching *WMAP* constraints on the optical depth with our model requires high average escape fractions of $f_{\rm esc} > 0.2$ during reionization (Section 6.2).

8. The *JWST* should see many $M_* > 10^8\, M_\odot$ galaxies over the entire redshift range $8 < z < 15$ (Section 6.3).

APPENDIX A

TESTS OF THE METHODOLOGY AT $Z = 0.1$

Because we used abundance modeling to calculate SMHM relations and SSFRs (Section 3.2) throughout this paper, it may seem that some of the simplicity of Section 2.1 has been lost. Here we show that the method still works without the extra machinery of Section 3.2, albeit with some cost to accuracy.

In the left panels of Figure 17, we show the SMHM ratios derived in Reddick et al. (2013), along with SSFRs from Salim et al. (2007). Reddick et al. (2013) derived their results from abundance matching the Moustakas et al. (2013) SMF at $z = 0.1$ to halos in the Bolshoi simulation (Section 3.3). The bottom two panels on the left of Figure 17 also show the specific halo mass accretion rates from Appendix B. These panels show the stark contrast between the formation of galaxies and halos at low redshifts: galaxies in low-mass halos are forming stars much more rapidly than their halos are growing, and the opposite is true for galaxies in high-mass halos.

In the right panels of Figure 17, we show predictions for the SMHM ratios at $z = 1$, 2, and 3 from using the Reddick et al. (2013) and Salim et al. (2007) data directly in Equations (2) and (4). We note that the stellar mass estimators used in Moustakas et al. (2013) and Salim et al. (2007) are different, each using SED fitting with their own stellar population history models and dust models. We also note that the Salim et al. (2007) SSFRs are the ratio of current SFR to currently remaining stellar mass, whereas Equation (4) requires the ratio of current SFR to the total stellar mass ever formed. For a 13 Gyr old population, the ratio of currently remaining to total formed stellar mass is 54% (Equation (6)), so we also show predictions if we multiply the Salim et al. (2007) SSFRs by this fraction. These predictions therefore bracket the range of allowable ages for stellar populations. We make no attempt to correct for stellar mass gained in mergers (Section 2.2). Behroozi et al. (2013c) find that the merger contribution is negligible for $M_h < 10^{12}\, M_\odot$ halos but can be important for $M_h > 10^{13.5}\, M_\odot$ halos at $z < 2$.

Nonetheless, this predictive range is in remarkable agreement with constraints from Behroozi et al. (2013c) at $z = 1$ and $z = 2$. We find it astonishing that the physical properties of galaxies three-quarters of the way back to the big bang are predictable using observations of practically our own backyard. The agreement at $z > 2$ is not so good, and it is worth understanding why the relationship breaks down at higher

redshifts. In fact, at low redshifts, a simple pure power-law star formation efficiency history like that assumed in Equation (2) is only a reasonable description for low-mass galaxies—i.e., galaxies with masses less than $10^{10.5}\, M_\odot$ in halos with masses less than $10^{12}\, M_\odot$. Predictions for high-mass galaxies work because their SSFRs are low. As long as the predicted SSFRs are less than the inverse Hubble time, huge relative errors no longer matter: the buildup of the galaxy stellar mass from $z = 2$ to $z = 0$ will be only a small fraction of the total (see also Equation (7)). However, at $z > 2$, many of the massive galaxies today were forming most of their stars (Behroozi et al. 2013c), and the growth of galaxies relative to their halos was much faster (e.g., Figure 4). Getting the magnitude of the SSFRs correct therefore becomes more important, and the simple extrapolation in Equation (2) breaks down.

APPENDIX B

CALIBRATING MASS ACCRETION RATES

We calculate halo mass accretion rates from the growth of halos between discrete simulation time steps. As usual, if the time steps are spaced too closely, halo growth will be small relative to measurement errors (e.g., Poisson noise and halo-finding algorithm instabilities). If the time steps are too far apart, the halo growth rate will change over the time interval, and the inferred rates will be biased. To work around this problem, we adopt a parameterized fitting function for the average halo growth rate. In this way, the inferred halo growth between any two redshifts can be checked for consistency with direct measurements from simulations.

The choice of fitting function is important, since we are modeling halo growth over large redshift ranges (e.g., $z = 8$ to $z = 15$). Common fitting forms (e.g., Wechsler et al. 2002; McBride et al. 2009; Wu et al. 2013) approximate the early growth of halos as exponential in redshift. While not a bad approximation at a single halo mass, halos at different masses will have different exponential growth rates. Since larger halos form later, their growth profiles are better fit by steeper exponential growth rates (Wechsler et al. 2002; McBride et al. 2009); extrapolating this faster growth to high redshifts results in the progenitor mass histories of high-mass halos unphysically falling below the progenitor mass histories of lower-mass halos.

Behroozi et al. (2013c) avoid this problem by fitting the growth history of halos at a single mass ($10^{13}\, M_\odot$) with a standard form and then fitting mass growth histories for other halo masses relative to the trajectory for $10^{13}\, M_\odot$ halos. This results in an accurate, although very complicated, fit for mass growth histories, which we reproduce here:

$$M_{\rm med}(M_0, z) = M_{13}(z) 10^{f(M_0, z)} \tag{B1}$$

$$M_{13}(z) = 10^{13.276}(1+z)^{3.00}\left(1+\frac{z}{2}\right)^{-6.11}$$
$$\times \exp(-0.503z)\, M_\odot \tag{B2}$$

$$f(M_0, z) = \log_{10}\left(\frac{M_0}{M_{13}(0)}\right)\frac{g(M_0, 1)}{g(M_0, \frac{1}{1+z})} \tag{B3}$$

$$g(M_0, a) = 1 + \exp(-4.651(a - a_0(M_0))) \tag{B4}$$

$$a_0(M_0) = 0.205 - \log_{10}\left[\left(\frac{10^{9.649}\, M_\odot}{M_0}\right)^{0.18} + 1\right], \tag{B5}$$
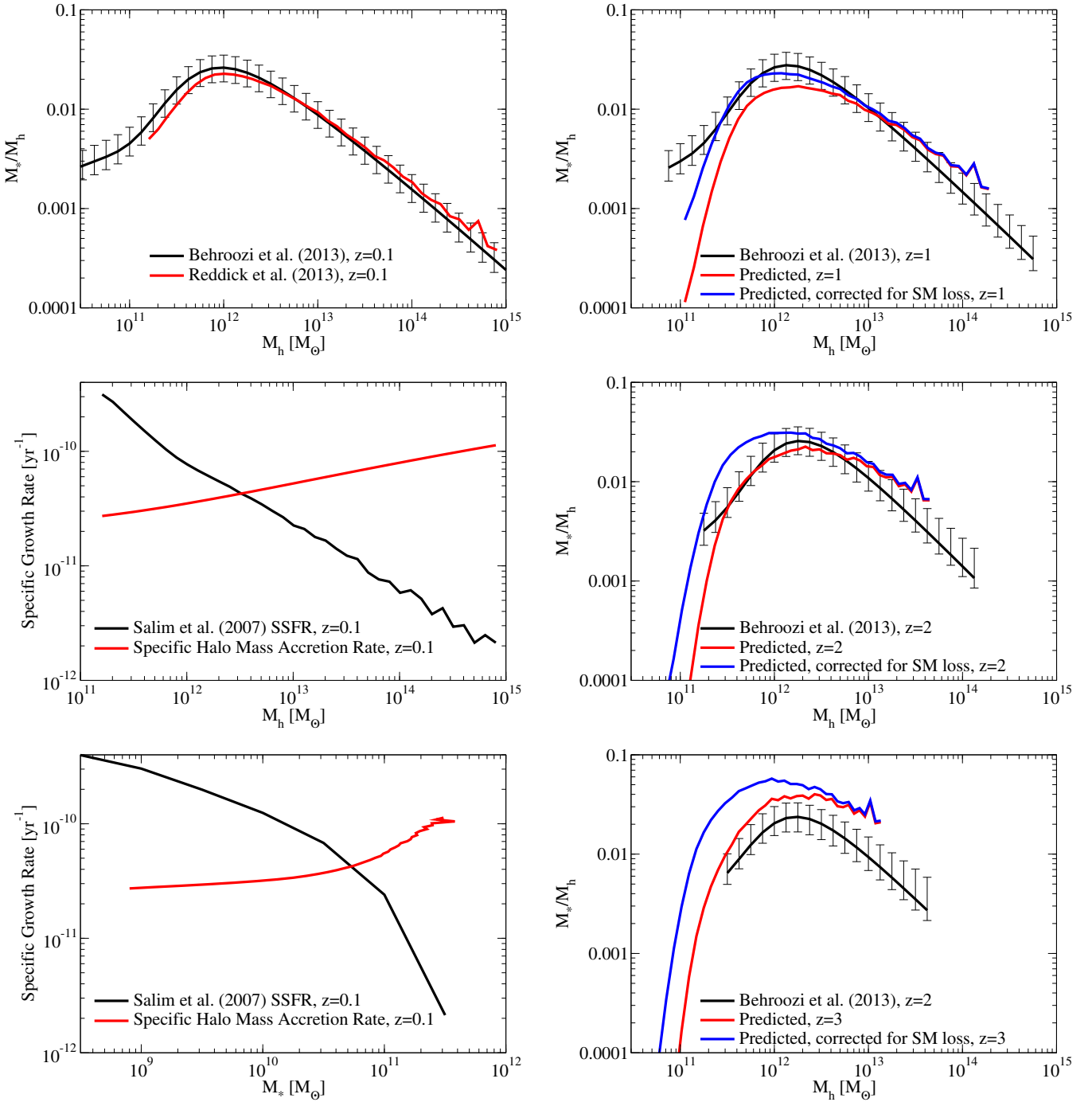
Figure 17. Test of the methodology in Section 2.1 at low redshifts. The top left panel shows the SMHM ratio for $z = 0.1$ derived in Reddick et al. (2013) by pure abundance matching (i.e., considering a single redshift only), compared to the SMHM ratio in Behroozi et al. (2013c), derived by abundance modeling (Section 3.2). The middle left panel shows the SSFRs from Salim et al. (2007) as a function of halo mass (using Reddick et al. 2013 to convert between stellar mass and halo mass) along with specific halo mass accretion rates as a function of halo mass (Appendix B). The bottom left panel shows the same data, except this time plotted as a function of stellar mass. The top right panel compares the Behroozi et al. (2013c) constraints on the SMHM ratio at $z = 1$ (black line) with predictions for the $z = 1$ SMHM ratio using the $z = 0.1$ Reddick et al. (2013) SMHM ratio and the Salim et al. (2007) SSFRs with the methodology in Section 2.1 (red line). The blue line shows the predictions if the Salim et al. (2007) SSFRs are not corrected for passive stellar mass loss (Section 2.2). The middle right and bottom right panels show the analogous comparisons at $z = 2$ and $z = 3$. As explained in the text, the assumption of a power-law historical SMHM relation for galaxies at $z = 0.1$ breaks down at $z = 2$ and above.

where $M(M_0, z)$ gives the median virial mass (Bryan & Norman 1998) for progenitors of halos with mass M_0 at $z = 0$.

Since we are interested in average accretion rates, instead of the growth of the median halo mass, we cannot use the values directly from this function. However, rather than refitting all the parameters, we consider simple modifications to the time

derivative of this function:

$$\langle \dot{M}_{\mathrm{peak}} \rangle (M_{\mathrm{peak}}, a) = \dot{M}_{\mathrm{med}}(M_0(M_{\mathrm{peak}}, a), a) F(M_{\mathrm{peak}}, a), \quad \text{(B6)}$$

where $M_0(M_{\mathrm{peak}}, a)$ is the inverse function of $M_{\mathrm{med}}(M_0, a)$, i.e., $M_{\mathrm{med}}(M_0(M_{\mathrm{peak}}, a), a) = M_{\mathrm{peak}}$.
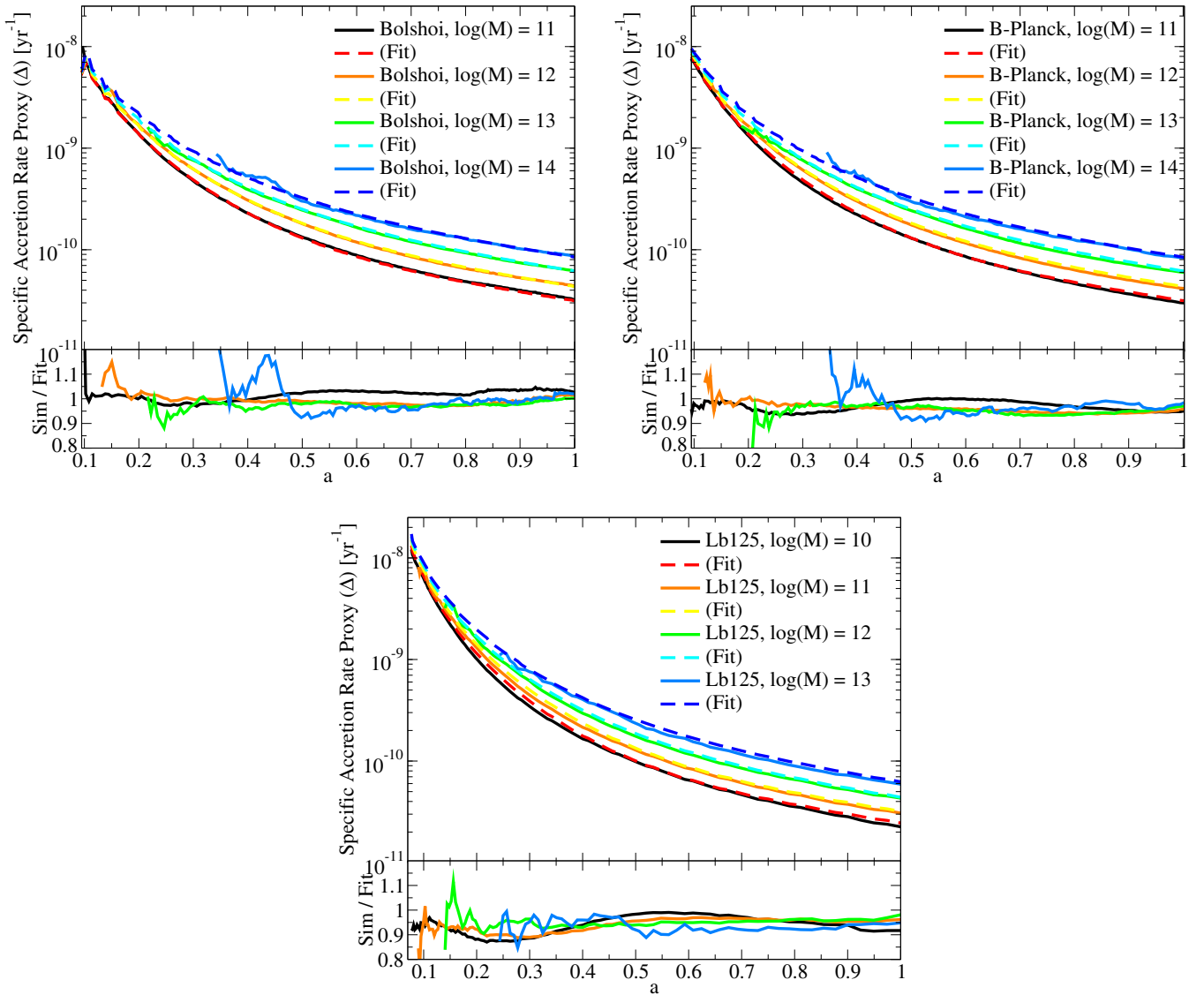
Figure 18. Left panel: SMARs as a function of halo mass and scale factor in the Bolshoi simulation (measured using the Δ proxy, Equation (B8)) compared with the Δ values from Equation (B8). The lower left panel shows the ratio of the values measured in the simulation to the fit; typical deviations are 2%–3%. Right panel: same as the left panel, but for the Bolshoi–Planck simulation, which uses a cosmology similar to the Planck best-fit values (Planck Collaboration et al. 2013). Bottom panel: same as the left panel, but for the *Lb125* simulation, which uses a cosmology in between the Bolshoi and Bolshoi–Planck cosmologies.

To compare with simulations, we have measured the following proxy for SMAR for every halo in Bolshoi for every time step redshift z:

$$\Delta = \frac{M_{\text{peak}}(z) - M_{\text{peak}}(z + 0.5)}{M_{\text{peak}}(z)[t(z) - t(z + 0.5)]}, \quad \text{(B7)}$$

where $t(z)$ is the time since the big bang at redshift z. Calculating mass growth over a redshift delta of 0.5 ensures a typical halo growth of 0.125 dex, which is well beyond the typical 1%–5% mass fluctuations expected for halo finder mass recovery (Behroozi et al. 2013e). When a time step at exactly $z + 0.5$ was not available, we used the closest time step available. Bolshoi has 180 time steps, which are spaced between 40 and 90 Myr apart, so this granularity becomes important at $z > 4$.

For each trial parameter set in Equation (B8), we calculated the expected values for Δ as a function of halo mass and redshift. We find that the following formula for average mass accretion

rates is the best match to the Bolshoi simulation:

$$\langle \dot{M}_{\text{peak}} \rangle (M_{\text{peak}}, a) = \dot{M}_{\text{med}}(M_0(M_{\text{peak}}, a), a)$$

$$\times [0.22(a - 0.4)^2 + 0.85] \frac{\left(\frac{M_{\text{peak}}}{10^{12} M_\odot} \right)^{0.05a}}{\left(1.0 + \frac{10^{11 - 0.5a} M_\odot}{M_{\text{peak}}} \right)^{0.04 + 0.1a}}. \quad \text{(B8)}$$

We show a comparison between this formula's expected values for Δ and the actual values in Bolshoi as a function of halo mass and redshift in the left panel of Figure 18. The fitting formula's typical deviations are 2%–3% from the measured values.

We have also checked this formula against two newer simulations. Bolshoi–Planck uses a cosmology ($\Omega_M = 0.307$, $\Omega_\Lambda = 0.693$, $h = 0.68$, $\sigma_8 = 0.823$, $n_s = 0.96$) similar to the Planck best-fit cosmology (Planck Collaboration et al. 2013). This simulation used the same box size (250 Mpc h^{-1}), particle number (2048^3), force resolution (1 kpc h^{-1}), and simulation code (ART) as Bolshoi. As noted in Section 5.3.2, this cosmology's SMARs are expected to be about 2% different
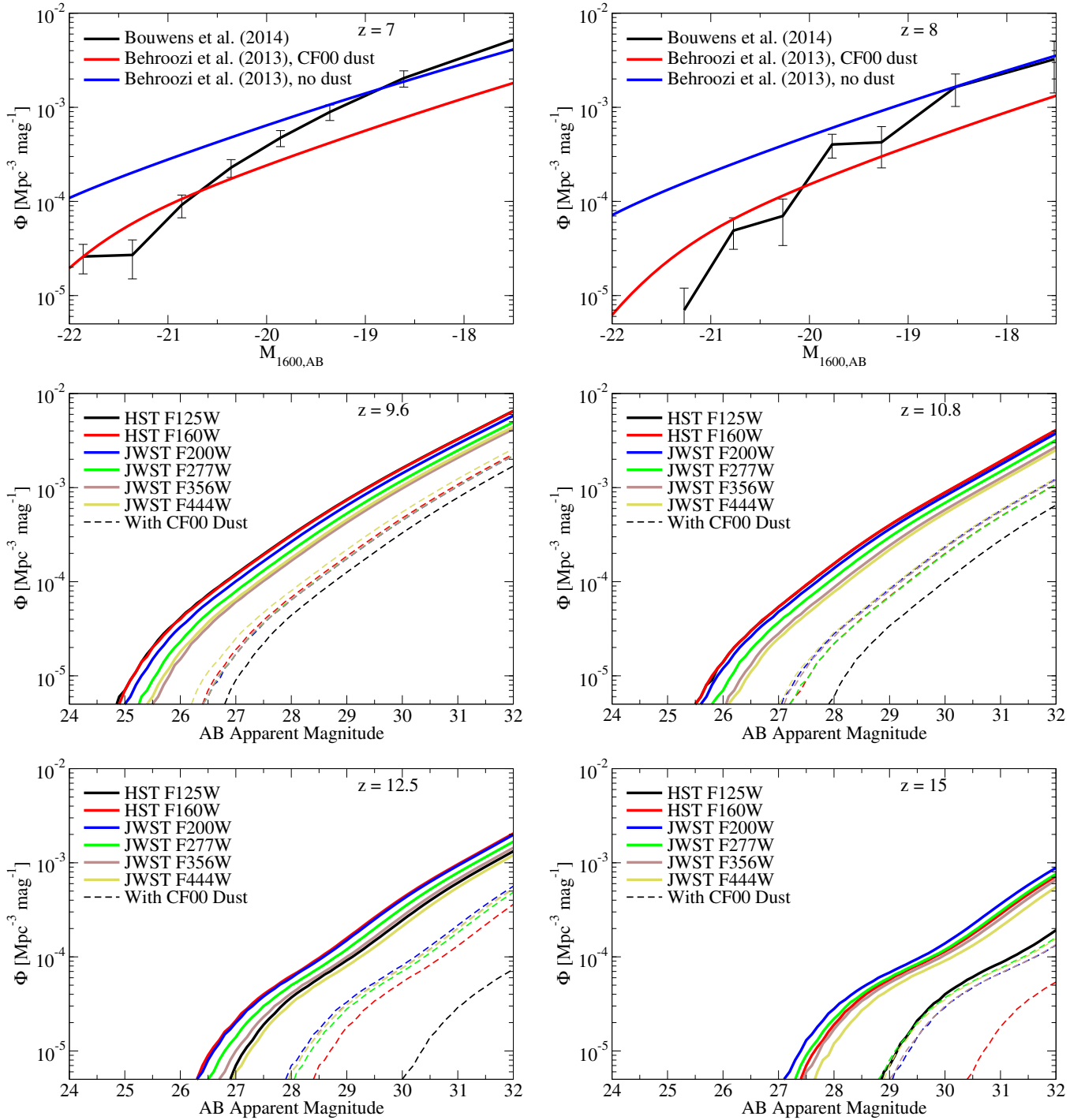
Figure 19. Luminosity functions at $z \geqslant 7$. Top panels: predicted UV luminosity functions at $z = 7$ and $z = 8$, compared to those in Bouwens et al. (2014c). Dust is a significant systematic uncertainty, and variation in dust with luminosity is the main reason why observed UV luminosity functions have steeper faint-end slopes than the corresponding SMFs. We show luminosity functions both with and without the addition of a Charlot & Fall (2000) dust model ("CF00"). Middle and bottom panels: predicted luminosity functions in several *HST* WFC3 (F125W and F160W) and *JWST* NIRCAM (F200W–F444W) filters, both without (solid lines) and with (dashed lines) a Charlot & Fall (2000) dust model. Even at $z = 15$, the Lyman break does not enter any of the *JWST* filters shown here. Error bars are not shown for clarity; systematic errors from the uncertainties in stellar mass growth histories are 0.75, 0.9, 1.25, and 1.75 mag at $z = 9.6$, 10.8, 12.5, and 15, respectively.

from that of the Bolshoi simulation. This expectation is borne out in the right panel of Figure 18, where the measured deviations from the fitting formula in Equation (B8) are 4%–5%. We also used the *Lb125* simulation to constrain the low-mass and high-redshift accretion rate behavior that is not as well sampled by Bolshoi. *Lb125* uses a cosmology in between the Bolshoi and Bolshoi–Planck cosmologies ($\Omega_M = 0.286$, $\Omega_\Lambda = 0.714$,

$h = 0.7$, $\sigma_8 = 0.82$, $n_s = 0.96$). This simulation used a smaller box size (125 Mpc h^{-1}), with the same particle number (2048^3) as Bolshoi but with slightly higher force resolution (Plummer equivalent of 0.5 kpc h^{-1}) and using the GADGET simulation code (Springel 2005). The smaller box size (and consequent lack of larger-scale modes) reduces average halo accretion rates at fixed halo mass to 90%–95% of those in Bolshoi.

APPENDIX C

LUMINOSITY FUNCTIONS

Since we use converted UV luminosity functions to constrain the growth of stellar mass at $z \geqslant 7$, it is important to check that the stellar mass growth we infer is self-consistent with the observed UV luminosity functions. We follow the same procedure for generating luminosities as in Behroozi et al. (2014a); specifically, we generate UV luminosity functions using the FSPS stellar population synthesis code (Conroy et al. 2010; Conroy & Gunn 2010) and assume that the metallicity of stars produced follows the extrapolated gas-phase metallicity as a function of stellar mass and redshift from Maiolino et al. (2008). Dust represents a significant uncertainty, however, as the only practical method for inferring the dust content of individual galaxies at $z > 7$ is to use the UV slope β (Bouwens et al. 2014b). We therefore show all results both with and without the effects of a Charlot & Fall (2000) dust model.

UV luminosity functions at $z = 7$ and $z = 8$ generated from the best-fit stellar growth models in Behroozi et al. (2013c) are shown in the top panels of Figure 19. As suggested by the evolution of β with luminosity, more luminous galaxies are likely dustier than fainter galaxies (Bouwens et al. 2014b). This seems in qualitative agreement with our generated luminosity functions, as the observations lie closer to the models including dust for bright galaxies and are closer to the models without dust for faint galaxies.

We have also generated apparent luminosity functions in several *HST* WFC3 (F125W and F160W) and *JWST* NIRCAM (F200W–F444W) filters from our predictions in Section 5, which appear in the bottom panels of Figure 19. If the dust–luminosity relation extends to higher redshifts, it is likely that the true luminosity functions will be closer to the models including dust for bright galaxies and closer to the models without dust for faint galaxies. However, we caution that the systematic errors from uncertainties in stellar mass growth histories are significant; these are 0.75, 0.9, 1.25, and 1.75 mag at $z = 9.6$, 10.8, 12.5, and 15, respectively.

REFERENCES

Agertz, O., Kravtsov, A. V., Leitner, S. N., & Gnedin, N. Y. 2013, ApJ, 770, 25
Aird, J., Nandra, K., Laird, E. S., et al. 2010, MNRAS, 401, 2531
Alvarez, M. A., Finlator, K., & Trenti, M. 2012, ApJL, 759, L38
Baldry, I. K., Glazebrook, K., & Driver, S. P. 2008, MNRAS, 388, 945
Behroozi, P. S., Conroy, C., & Wechsler, R. H. 2010, ApJ, 717, 379
Behroozi, P. S., Marchesini, D., Wechsler, R. H., et al. 2013a, ApJL, 777, L10
Behroozi, P. S., Ramirez-Ruiz, E., & Fryer, C. L. 2014a, ApJ, 792, 123
Behroozi, P. S., Wechsler, R. H., & Conroy, C. 2013b, ApJL, 762, L31
Behroozi, P. S., Wechsler, R. H., & Conroy, C. 2013c, ApJ, 770, 57
Behroozi, P. S., Wechsler, R. H., Lu, Y., et al. 2014b, ApJ, 787, 156
Behroozi, P. S., Wechsler, R. H., & Wu, H.-Y. 2013d, ApJ, 762, 109
Behroozi, P. S., Wechsler, R. H., Wu, H.-Y., et al. 2013e, ApJ, 763, 18
Bennett, C. L., Larson, D., Weiland, J. L., et al. 2013, ApJS, 208, 20
Bernardi, M., Shankar, F., Hyde, J. B., et al. 2010, MNRAS, 404, 2087
Béthermin, M., Doré, O., & Lagache, G. 2012, A&A, 537, L5
Bonnell, I. A., Larson, R. B., & Zinnecker, H. 2007, Protostars and Planets V,
    ed. B. Reipurth, D. Jewitt, & K. Keil (Tucson, AZ: Univ. Arizona Press), 149
Bouwens, R., Bradley, L., Zitrin, A., et al. 2014a, ApJ, 795, 126
Bouwens, R. J., Illingworth, G. D., Oesch, P. A., et al. 2011, ApJ, 737, 90
Bouwens, R. J., Illingworth, G. D., Oesch, P. A., et al. 2012a, ApJ, 754, 83
Bouwens, R. J., Illingworth, G. D., Oesch, P. A., et al. 2012b, ApJL, 752, L5
Bouwens, R. J., Illingworth, G. D., Oesch, P. A., et al. 2014b, ApJ, 793, 115
Bouwens, R. J., Illingworth, G. D., Oesch, P. A., et al. 2014c, arXiv:1403.4295
Boylan-Kolchin, M., Bullock, J. S., & Kaplinghat, M. 2012, MNRAS,
    422, 1203
Bradley, L. D., Trenti, M., Oesch, P. A., et al. 2012, ApJ, 760, 108
Brammer, G. B., Whitaker, K. E., van Dokkum, P. G., et al. 2011, ApJ, 739, 24
Bromm, V., & Yoshida, N. 2011, ARA&A, 49, 373
Bryan, G. L., & Norman, M. L. 1998, ApJ, 495, 80
Castellano, M., Sommariva, V., Fontana, A., et al. 2014, A&A, 566, A19
Chabrier, G. 2003, PASP, 115, 763
Charlot, S., & Fall, S. M. 2000, ApJ, 539, 718
Chen, C.-T. J., Hickox, R. C., Alberts, S., et al. 2013, ApJ, 773, 3
Coe, D., Zitrin, A., Carrasco, M., et al. 2013, ApJ, 762, 32
Conroy, C., & Gunn, J. E. 2010, ApJ, 712, 833
Conroy, C., Gunn, J. E., & White, M. 2009, ApJ, 699, 486
Conroy, C., Wechsler, R. H., & Kravtsov, A. V. 2006, ApJ, 647, 201
Conroy, C., & White, M. 2013, ApJ, 762, 70
Conroy, C., White, M., & Gunn, J. E. 2010, ApJ, 708, 58
Cucciati, O., Tresse, L., Ilbert, O., et al. 2012, A&A, 539, A31
Curtis-Lake, E., McLure, R. J., Dunlop, J. S., et al. 2013, MNRAS, 429, 302
Daddi, E., Dickinson, M., Morrison, G., et al. 2007, ApJ, 670, 156
Dayal, P., Dunlop, J. S., Maio, U., & Ciardi, B. 2013, MNRAS, 434, 1486
de Barros, S., Schaerer, D., & Stark, D. P. 2014, A&A, 563, A81
Dijkstra, M., Wyithe, S., Haiman, Z., Mesinger, A., & Pentericci, L.
    2014, MNRAS, 440, 3309
Duncan, K., Conselice, C. J., Mortlock, A., et al. 2014, MNRAS, 444, 2960
Dunne, L., Ivison, R. J., Maddox, S., et al. 2009, MNRAS, 394, 3
Ellis, R. S., McLure, R. J., Dunlop, J. S., et al. 2013, ApJL, 763, L7
Fakhouri, O., & Ma, C. 2008, MNRAS, 386, 577
Fakhouri, O., Ma, C.-P., & Boylan-Kolchin, M. 2010, MNRAS, 406, 2267
Feulner, G., Gabasch, A., Goranova, Y., Hopp, U., & Bender, R. 2008,
    in Relativistic Astrophysics Legacy and Cosmology—Einstein's, ed. B.
    Aschenbach, V. Burwitz, G. Hasinger, & B. Leibundgut (Berlin: Springer-
    Verlag), 310
Finlator, K., Davé, R., & Özel, F. 2011, ApJ, 743, 169
Gardner, J. P., Mather, J. C., Clampin, M., et al. 2006, SSRv, 123, 485
Gnedin, N. Y. 2000, ApJ, 542, 535
González, V., Bouwens, R., Illingworth, G., et al. 2014, ApJ, 781, 34
González, V., Labbé, I., Bouwens, R. J., et al. 2011, ApJL, 735, L34
Governato, F., Zolotov, A., Pontzen, A., et al. 2012, MNRAS, 422, 1231
Grazian, A., Fontana, A., Santini, P., et al. 2014, arXiv:1412.0532
Haardt, F., & Madau, P. 2012, ApJ, 746, 125
Habergham, S. M., Anderson, J. P., & James, P. A. 2010, ApJ, 717, 342
Hayes, M., Schaerer, D., Östlin, G., et al. 2011, ApJ, 730, 8
Hickox, R. C., Mullaney, J. R., Alexander, D. M., et al. 2014, ApJ, 782, 9
Hopkins, A. M., & Beacom, J. F. 2006, ApJ, 651, 142
Jaacks, J., Choi, J.-H., Nagamine, K., Thompson, R., & Varghese, S.
    2012a, MNRAS, 420, 1606
Jaacks, J., Nagamine, K., & Choi, J. H. 2012b, MNRAS, 427, 403
Kajisawa, M., Ichikawa, T., Yamada, T., et al. 2010, ApJ, 723, 129
Karim, A., Schinnerer, E., Martnez-Sansigre, A., et al. 2011, ApJ, 730, 61
Kistler, M. D., Yüksel, H., Beacom, J. F., Hopkins, A. M., & Wyithe, J. S. B.
    2009, ApJL, 705, L104
Kistler, M. D., Yuksel, H., & Hopkins, A. M. 2013, arXiv:1305.1630
Klypin, A. A., Trujillo-Gomez, S., & Primack, J. 2011, ApJ, 740, 102
Knebe, A., Knollmann, S. R., Muldrew, S. I., et al. 2011, MNRAS, 415, 2293
Knebe, A., Pearce, F. R., Lux, H., et al. 2013, MNRAS, 435, 1618
Kravtsov, A., & Klypin, A. 1999, ApJ, 520, 437
Kravtsov, A. V., Klypin, A. A., & Khokhlov, A. M. 1997, ApJ, 111, 73
Labbé, I., Oesch, P. A., Bouwens, R. J., et al. 2013, ApJL, 777, L19
Lacey, C. G., Baugh, C. M., Frenk, C. S., & Benson, A. J. 2011, MNRAS,
    412, 1828
Le Borgne, D., Elbaz, D., Ocvirk, P., & Pichon, C. 2009, A&A, 504, 727
Leauthaud, A., Tinker, J., Bundy, K., et al. 2012, ApJ, 744, 159
Lee, K.-S., Dey, A., Reddy, N., et al. 2011, ApJ, 733, 99
Lee, K.-S., Ferguson, H. C., Wiklind, T., et al. 2012, ApJ, 752, 66
Lee, K.-S., Giavalisco, M., Conroy, C., et al. 2009, ApJ, 695, 368
Lee, S.-K., Ferguson, H. C., Somerville, R. S., et al. 2014, ApJ, 783, 81
Leitner, S. N. 2012, ApJ, 745, 149
Loeb, A., & Barkana, R. 2001, ARA&A, 39, 19
Lu, Z., Mo, H. J., Lu, Y., et al. 2014, MNRAS, 439, 1294
Ly, C., Lee, J. C., Dale, D. A., et al. 2011a, ApJ, 726, 109
Ly, C., Malkan, M. A., Hayashi, M., et al. 2011b, ApJ, 735, 91
Madau, P., & Dickinson, M. 2014, ARA&A, 52, 415
Magnelli, B., Elbaz, D., Chary, R. R., et al. 2011, A&A, 528, A35
Maiolino, R., Nagao, T., Grazian, A., et al. 2008, A&A, 488, 463
Marchesini, D., van Dokkum, P. G., Förster Schreiber, N. M., et al. 2009, ApJ,
    701, 1765
Marchesini, D., Whitaker, K. E., Brammer, G., et al. 2010, ApJ, 725, 1277
Marks, M., Kroupa, P., Dabringhausen, J., & Pawlowski, M. S. 2012, MNRAS,
    422, 2246
McBride, J., Fakhouri, O., & Ma, C.-P. 2009, MNRAS, 398, 1858
McLure, R. J., Dunlop, J. S., de Ravel, L., et al. 2011, MNRAS, 418, 2074

More, S., van den Bosch, F. C., Cacciato, M., et al. 2009, MNRAS, 392, 801
Mortlock, A., Conselice, C. J., Bluck, A. F. L., et al. 2011, MNRAS, 413, 2845
Moster, B. P., Naab, T., & White, S. D. M. 2013, MNRAS, 428, 3121
Moster, B. P., Somerville, R. S., Maulbetsch, C., et al. 2010, ApJ, 710, 903
Moustakas, J., Coil, A. L., Aird, J., et al. 2013, ApJ, 767, 50
Mullaney, J. R., Daddi, E., Béthermin, M., et al. 2012, ApJL, 753, L30
Muzzin, A., Marchesini, D., Stefanon, M., et al. 2013, ApJ, 777, 18
Narayanan, D., & Davé, R. 2013, MNRAS, 436, 2892
Noeske, K. G., Weiner, B. J., Faber, S. M., et al. 2007, ApJL, 660, L43
Noh, Y., & McQuinn, M. 2014, MNRAS, 444, 503
Oesch, P. A., Bouwens, R. J., Illingworth, G. D., et al. 2014a, arXiv:1409.1228
Oesch, P. A., Bouwens, R. J., Illingworth, G. D., et al. 2014b, ApJ, 786, 108
Papovich, C., Finkelstein, S. L., Ferguson, H. C., Lotz, J. M., & Giavalisco, M.
    2011, MNRAS, 412, 1123
Pérez-González, P. G., Rieke, G. H., Villar, V., et al. 2008, ApJ, 675, 234
Planck Collaboration, Ade, P. A. R., Aghanim, N., et al. 2013, A&A, 571, A16
Pontzen, A., & Governato, F. 2014, Natur, 506, 171
Reddick, R. M., Wechsler, R. H., Tinker, J. L., & Behroozi, P. S. 2013, ApJ,
    771, 30
Reddy, N. A., Pettini, M., Steidel, C. C., et al. 2012, ApJ, 754, 25
Reddy, N. A., & Steidel, C. C. 2009, ApJ, 692, 778
Robertson, B. E., & Ellis, R. S. 2012, ApJ, 744, 95
Robertson, B. E., Furlanetto, S. R., Schneider, E., et al. 2013, ApJ, 768, 71
Robotham, A. S. G., & Driver, S. P. 2011, MNRAS, 413, 2570
Rujopakarn, W., Eisenstein, D. J., Rieke, G. H., et al. 2010, ApJ, 718, 1171
Salim, S., Rich, R. M., Charlot, S., et al. 2007, ApJS, 173, 267
Salmi, F., Daddi, E., Elbaz, D., et al. 2012, ApJL, 754, L14
Salpeter, E. E. 1955, ApJ, 121, 161
Scalo, J. 2005, in Astrophysics and Space Science Library, Vol. 327, The Initial
    Mass Function 50 Years Later, ed. E. Corbelli, F. Palla, & H. Zinnecker
    (Dordrecht: Springer), 23
Schaerer, D., & de Barros, S. 2010, A&A, 515, A73
Schmidt, K. B., Treu, T., Trenti, M., et al. 2014, ApJ, 786, 57
Shim, H., Colbert, J., Teplitz, H., et al. 2009, ApJ, 696, 785
Shimizu, I., & Inoue, A. K. 2013, PASJ, 65, 96
Silverman, J. D., Green, P. J., Barkhouse, W. A., et al. 2008, ApJ, 679, 118
Smolčić, V., Schinnerer, E., Zamorani, G., et al. 2009, ApJ, 690, 610
Sobral, D., Smail, I., Best, P. N., et al. 2013, MNRAS, 428, 1128
Spergel, D., Flauger, R., & Hlozek, R. 2013, arXiv:1312.3313
Springel, V. 2005, MNRAS, 364, 1105

Stark, D. P., Ellis, R. S., Bunker, A., et al. 2009, ApJ, 697, 1493
Stark, D. P., Schenker, M. A., Ellis, R., et al. 2013, ApJ, 763, 129
Tacchella, S., Trenti, M., & Carollo, C. M. 2013, ApJL, 768, L37
Tadaki, K.-I., Kodama, T., Koyama, Y., et al. 2011, PASJ, 63, 437
Teyssier, R., Pontzen, A., Dubois, Y., & Read, J. I. 2013, MNRAS, 429, 3068
Tinker, J., Kravtsov, A. V., Klypin, A., et al. 2008, ApJ, 688, 709
Tinker, J. L., Leauthaud, A., Bundy, K., et al. 2013, ApJ, 778, 93
Trenti, M., & Stiavelli, M. 2008, ApJ, 676, 767
Trenti, M., Stiavelli, M., Bouwens, R. J., et al. 2010, ApJL, 714, L202
Twite, J. W., Conselice, C. J., Buitrago, F., et al. 2012, MNRAS, 420, 1061
van der Burg, R. F. J., Hildebrandt, H., & Erben, T. 2010, A&A, 523, A74
Wang, F. Y. 2013, A&A, 556, A90
Wang, L., Farrah, D., Oliver, S. J., et al. 2013, MNRAS, 431, 648
Wardlow, J. L., Malhotra, S., Zheng, Z., et al. 2014, ApJ, 787, 9
Watson, D. F., & Conroy, C. 2013, ApJ, 772, 139
Watson, W. A., Iliev, I. T., D'Aloisio, A., et al. 2013, MNRAS, 433, 1230
Wechsler, R. H., Bullock, J. S., Primack, J. R., Kravtsov, A. V., & Dekel, A.
    2002, ApJ, 568, 52
Weidner, C., Kroupa, P., & Pflamm-Altenburg, J. 2011, MNRAS, 412, 979
Weinmann, S. M., Neistein, E., & Dekel, A. 2011, MNRAS, 417, 2737
Wetzel, A. R., Tinker, J. L., Conroy, C., & van den Bosch, F. C. 2013, MNRAS,
    432, 336
Whitaker, K. E., van Dokkum, P. G., Brammer, G., & Franx, M. 2012, ApJL,
    754, L29
Wise, J. H., Abel, T., Turk, M. J., Norman, M. L., & Smith, B. D.
    2012a, MNRAS, 427, 311
Wise, J. H., & Cen, R. 2009, ApJ, 693, 984
Wise, J. H., Demchenko, V. G., Halicek, M. T., et al. 2014, MNRAS,
    442, 2560
Wise, J. H., Turk, M. J., Norman, M. L., & Abel, T. 2012b, ApJ, 745, 50
Wu, H.-Y., Hahn, O., Wechsler, R. H., Mao, Y.-Y., & Behroozi, P. S. 2013, ApJ,
    763, 70
Wyithe, J. S. B., Loeb, A., & Oesch, P. A. 2014, MNRAS, 439, 1326
Yang, X., Mo, H. J., & van den Bosch, F. C. 2009, ApJ, 693, 830
Yang, X., Mo, H. J., van den Bosch, F. C., Zhang, Y., & Han, J. 2012, ApJ,
    752, 41
Yoshida, M., Shimasaku, K., Kashikawa, N., et al. 2006, ApJ, 653, 988
Zheng, W., Shu, X., Moustakas, J., et al. 2014, ApJ, 795, 93
Zheng, X. Z., Bell, E. F., Papovich, C., et al. 2007, ApJL, 661, L41
Zolotov, A., Brooks, A. M., Willman, B., et al. 2012, ApJ, 761, 71